Cite as: C. E. Nelson *et al.*, *Sci. Immunol.* 10.1126/sciimmunol.abo0535 (2022).

CORONAVIRUS

Mild SARS-CoV-2 infection in rhesus macaques is associated with viral control prior to antigen-specific T cell responses in tissues

Christine E. Nelson[1], Sivaranjani Namasivayam[2], Taylor W. Foreman[1], Keith D. Kauffman[1], Shunsuke Sakai[1], Danielle E. Dorosky[1], Nickiana E. Lora[1], NIAID/DIR Tuberculosis Imaging Program[3]†, Kelsie Brooks[4], E. Lake Potter[5], Nicole L. Garza[6], Bernard A. P. Lafont[6], Reed F. Johnson[6], Mario Roederer[5], Alan Sher[2], Daniela Weiskopf[7], Alessandro Sette[7,8], Emmie de Wit[9], Heather D. Hickman[10], Jason M. Brenchley[4], Laura E. Via[11,12], Daniel L. Barber[1]*

[1]T lymphocyte Biology Section, Laboratory of Parasitic Diseases, National Institutes of Allergy and Infectious Disease, National Institutes of Health, Bethesda, MD, USA. [2]Immunobiology Section, Laboratory of Parasitic Diseases, National Institutes of Allergy and Infectious Disease, National Institutes of Health, Bethesda, MD, USA. [3]Division of Intramural Research, National Institutes of Allergy and Infectious Disease, National Institutes of Health, Bethesda, MD, USA. [4]Barrier Immunity Section, Laboratory of Viral Diseases, National Institutes of Allergy and Infectious Disease, National Institutes of Health, Bethesda, MD, USA. [5]ImmunoTechnology Section, Vaccine Research Center, National Institutes of Allergy and Infectious Disease, National Institutes of Health, Bethesda, MD, USA. [7]Center for Infectious Disease and Vaccine Research, La Jolla Institute for Immunology, La Jolla, CA 92037, USA. [6]SARS-CoV-2 Virology Core, Laboratory of Viral Diseases, National Institute of Allergy and Infectious Diseases, National Institutes of Health, Bethesda, MD. [8]Department of Medicine, Division of Infectious Diseases and Global Public Health, University of California, San Diego (UCSD), La Jolla, CA 92037, USA. [9]Laboratory of Virology, Division of Intramural Research, National Institutes of Allergy and Infectious Disease, National Institutes of Health, Hamilton, MT, USA. [10]Viral Immunity and Pathogenesis Unit, Laboratory of Clinical Immunology and Microbiology, National Institutes of Allergy and Infectious Disease, National Institutes of Health, Bethesda, MD, USA. [11]Tuberculosis Research Section, Laboratory of Clinical Infectious Diseases, National Institutes of Allergy and Infectious Disease, National Institutes of Health, Bethesda, MD, USA. [12]Institute of Infectious Disease & Molecular Medicine and Division of Immunology, Department of Pathology, University of Cape Town, Observatory, South Africa.

†Members of the NIAID/DIR Tuberculosis Imaging Program are listed in the Acknowledgments.

***Corresponding author. Email: barberd@niaid.nih.gov**

SARS-CoV-2 primarily replicates in mucosal sites, and more information is needed about immune responses in infected tissues. Here, we used rhesus macaques to model protective primary immune responses in tissues during mild COVID-19. Viral RNA levels were highest on days 1-2 post-infection and fell precipitously thereafter. ^{18}F-fluorodeoxyglucose (FDG)-avid lung abnormalities and interferon (IFN)-activated monocytes and macrophages in the bronchoalveolar lavage (BAL) were found on days 3-4 post-infection. Virus-specific effector CD8$^+$ and CD4$^+$ T cells became detectable in the BAL and lung tissue on days 7-10, after viral RNA, radiologic evidence of lung inflammation, and IFN-activated myeloid cells had substantially declined. Notably, SARS-CoV-2-specific T cells were not detectable in the nasal turbinates, salivary glands, and tonsils on day 10 post-infection. Thus, SARS-CoV-2 replication wanes in the lungs of rhesus macaques prior to T cell responses, and in the nasal and oral mucosa despite the apparent lack of antigen-specific T cells, suggesting that innate immunity efficiently restricts viral replication during mild COVID-19.

INTRODUCTION

SARS-CoV-2 infection has a spectrum of clinical outcomes, ranging from asymptomatic to fatal. There is a need to parse out the role of individual immune cell types and molecular pathways that contribute to effective control of viral infection in asymptomatic/mild disease and those leading to organ failure during severe COVID-19. Increased pro-inflammatory cytokines (*1*–*3*), deficient type I interferon (IFN) responses (*4*–*6*), activation of inflammasomes (*7*), neutrophils (*8*–*10*), and monocytes/macrophages (*3*, *10*–*14*) have all been associated with severe COVID-19. Coordinated activation of CD8$^+$ and CD4$^+$ T cells, T cell activation state, and antigen (Ag) specificity have all been linked to favorable outcomes of SARS-CoV-2 infection (*15*–*20*). While neutralizing antibodies are clearly protective in immune hosts, T cell responses may also contribute to the protection provided by vaccination and natural infection (*21*–*24*).

Most studies of immune correlates of COVID-19 disease severity in humans have focused on sampling of peripheral blood. Nevertheless, some studies have observed infiltration of immune cells into the bronchoalveolar lavage (BAL) fluid, post-mortem lung tissue acquired from fatal COVID-19 cases, or from individuals undergoing medically necessary procedures (*12*, *14*, *25*, *26*). Notably, on autopsy, several reports

have observed a surprising lack of immune cells infiltrating into extrapulmonary tissues despite the presence of high levels of virus (*27–31*). These data highlight the importance of understanding the early host response in pulmonary and extrapulmonary tissues in the first few days after SARS-CoV-2 infection.

Animal models can be employed to obtain a detailed understanding of the host response in infected tissues. Studies in SARS-CoV-2 susceptible species provide insights into COVID-19 disease pathogenesis. For example, transgenic mouse strains expressing human angiotensin converting enzyme (ACE)2 (K18-hACE2), and mice induced to express hACE2 with viral vectors, are highly susceptible to SARS-CoV-2 infection (*32–36*). Syrian hamsters and ferrets are also moderately susceptible and shed infectious virus (*37–41*). On the other hand, species more resistant to SARS-CoV-2 disease are useful tools in examining mechanisms of efficient control of viral replication. Several non-human primate (NHP) species can be experimentally infected with SARS-CoV-2. Rhesus macaques, cynomolgus macaques, and African green monkeys typically develop mild symptoms after SARS-CoV-2 infection (*42–52*). SARS-CoV-2 immune and vaccinated rhesus macaques are protected from reinfection primarily by neutralizing antibodies and to a lesser extent anamnestic T cell responses (*53–64*). Thus, current NHP models are suitable for the study of protective host immune responses associated with mild SARS-CoV-2 infection, but not the mechanisms of pathogenesis during severe disease.

In this study, we use the rhesus macaque model of mild COVID-19 to examine the (1) kinetics of lung inflammation using ^{18}FDG positron emission tomography computed tomography (PET/CT) imaging, (2) innate immune responses using single cell RNA sequencing (scRNAseq), and (3) the tissue distribution of SARS-CoV-2-specific T cell responses by flow cytometry. Our findings suggest that mild SARS-CoV-2 disease and efficient control of the infection are temporally correlated with activation of myeloid cells by type I IFN, prior to the induction of Ag-specific T and B cell responses. Moreover, they reveal a strong propensity for Ag-specific T cell migration into the pulmonary compartment compared to other mucosal sites of infection.

RESULTS

Radiologic and virological outcomes of SARS-CoV-2 infection in rhesus macaques

Six, male rhesus macaques were infected with 1x10^6 tissue culture infectious dose (TCID)$_{50}$ intranasally (i.n.) and 1x10^6 TCID$_{50}$ intratracheally (i.t.), for a total dose of 2x10^6 TCID$_{50}$ of SARS-CoV-2/USA-WA-1 (Table S1). ^{18}FDG PET/CT imaging showed evidence of heterogeneous inflammatory foci with increased ^{18}FDG uptake (Fig. 1A, B) and lesion density (Fig. 1A, C) in the lungs of 5 of 6 animals at day 3 post-infection, which resolved by day 9. Total genomic Nucleocapsid (gN) and subgenomic Nucleocapsid (sgN) RNA levels from nasal and throat swabs peaked 1 to 2 days post-infection and decreased to undetectable levels by day 7 to 10 (Fig. 1D). Viral RNA was also found in the BAL of all animals at day 4 post-infection and was mostly cleared by day 7-10. It should be noted that day 4 post-infection likely does not represent the peak of viremia in the BAL, and previous studies indicate peak viral loads are reached at day 1 post-infection in the BAL (*42*). Viral RNA was essentially absent from plasma at all timepoints, consistent with previous reports (*42*).

The animals were necropsied at day 10 post-infection for tissue analysis. A 3D reconstruction of the day 3 PET/CT images with conducting airways was used to locate and individually collect the previously PET hot lung regions and normal lung tissue separately. SARS-CoV-2 gN RNA was found on day 10 in all secondary lymphoid organs (SLO) and non-lymphoid tissues (NLT) tested, including the previously PET hot and normal lung tissue, nasal turbinates, salivary gland, and tonsils (Fig. 1E). sgN RNA was present at lower levels compared to gN RNA and was highest in lung tissue (Fig. 1F). The persistence of viral RNA at day 10, was confirmed with RNA scope immunohistochemical analysis (Fig. 1G). There was a correlation between genomic and subgenomic RNA levels in the mucosal swabs, BAL, and tissues with detectable RNA (Fig S1A-C). We did not observe a correlation between lung lesion severity at day 3 and viral RNA levels from nasal swabs and BAL at day 1 and 4, respectively (Fig S1D-G). Consistent with previous reports in macaques, various forms of CD62P$^+$ and fibrin$^+$ microthrombi were still detectable in the lungs on day 10 post-infection (Fig. 1H) (*44*). Thus, in rhesus macaques SARS-CoV-2 viral loads peak in the upper airways ~1-2 days after exposure and this results in mild and transient radiographic evidence of lung inflammation at ~3 days post-infection, with residual viral RNA in tissues and microthrombi in the lungs at day 10.

Longitudinal scRNAseq analysis of BAL and PBMC

To compare cellular immune responses in circulation versus airways, scRNAseq was performed on cryopreserved peripheral blood mononuclear cells (PBMC) and BAL samples obtained prior to infection and at days 4, 7 and 10 post-infection. Uniform manifold approximation and projection (UMAP) and nearest neighbor clustering of PBMCs from all timepoints identified multiple myeloid and T/NK cell populations along with B cells, platelets, and a mixture of proliferating cells (Fig. 2A). Due to PBMC isolation and cryopreservation, granulocyte populations were not accounted for in this study. Myeloid and T/NK cell populations were selected for subsequent clustering. We identified nine distinct T/NK cell subsets in PBMCs across all timepoints (Fig S2). Overall, we did not detect major alterations in the T/NK cell composition from PBMCs, but at day 4 after infection, we did observe a drop in naïve CD8$^+$ T cells and an increase in

central memory CD4$^+$ T cells (PBMC T/NK subpopulation 3 and 1, respectively) (Fig S2). Further clustering of myeloid cells identified seven distinct myeloid subsets in PBMCs (Fig. 2B-C). Most strikingly, there were major changes to CD14$^+$ monocytes after infection. At baseline, a subpopulation of CD14$^+$ monocytes expressing *PGTS2* (PBMC myeloid subpopulation 3) were predominant (Fig. 2C-D). At day 4 post-infection, there was a dramatic loss of the *PGTS2*$^+$ monocytes with an accompanying increase in two inflammatory monocyte populations with IFN-responsive gene signatures (PBMC myeloid subpopulation 0 and 1) (Fig. 2C-F). PBMC myeloid population 1 had a more prominent expression pattern of IFN-stimulated genes at day 4 as compared to PBMC myeloid population 0, i.e., *MX1*, *MX2*, *IFI6*, *IFI16*, *IFI27*, *ISG15*, and *OAS2*, although both populations showed evidence of response to IFN (Fig. 2B, E-F). In contrast to the major changes in CD14$^+$ monocytes, CD16$^+$ monocytes (PBMC myeloid population 5) did not increase in relative abundance after infection (Fig. 2B-D).

An increase in certain subsets of dendritic cells (DC)2 have been associated with moderate/severe disease in COVID-19 patients (*65*, *66*). At day 4 post-infection we observed an increase in CD1c$^+$ conventional DC2s (cDC2 (*67*)) (PBMC myeloid subpopulation 4), which contracted by day 10. Conventional DC1 cells (*XCR1*, *BATF3* -expressing PBMC myeloid population 6) were less abundant than cDC2s and changed relatively little in abundance during infection. The major alterations in the CD14$^+$ monocytes substantially declined by day 7 post-infection and returned to baseline levels by day 10 (Fig. 2C-D). The *PGTS2*-expressing monocytes that were lost at day 4 returned by day 10 post-infection and did not show major changes in gene expression (Fig. 2C-D, G).

In the BAL, multiple distinct T cell and myeloid populations were identified, along with proliferating cells, B cells, plasmacytoid DCs (pDC), MAST cells, and epithelial cells (Fig. 3A). Further clustering of BAL T cells identified 5 populations of T cells (Fig S2D). The largest change was the appearance on day 4 of a population with a mixture of CD8$^+$ and CD4$^+$ T cells that had a prominent IFN-stimulated gene signature (BAL T cell sub population 3) (Fig S2D-F). These IFN-activated T cells were no longer detectable by day 7 post-infection. Further clustering of BAL myeloid cells revealed 10 distinct populations of myeloid cells (Fig. 3B-C). At baseline, BAL cells were mostly comprised of multiple MRC1$^+$MARCO$^+$ myeloid subsets (BAL myeloid subpopulations 0, 2, and 3) which are likely alveolar macrophages (Fig. 3C). At day 4 post-infection, there were major increases in populations of IFN-activated monocytes and macrophages in the BAL (BAL myeloid subpopulation 1 and 6), which declined by day 7 and returned to baseline levels by day 10 (Fig. 3B-D). At day 10 post-infection, the myeloid cells in the BAL were dominated by a population of CD1c$^+$ cDC2s (BAL myeloid sub population 4) (Fig. 3C). The cDC2 in the BAL had a pattern of differentially expressed genes that suggested that this population also responded to infection by upregulating type I IFN-responsive genes at day 4 post-infection (Fig. 3E). By day 10 the cDC2 had down regulated the type I IFN genes and up-regulated genes associated with responses to lipopolysaccharide (LPS), including additional chemokines and *IL1B*, as well as the macrophage markers *MRC1* and *MARCO*.

Correlation analysis revealed strong positive correlations between viral RNA levels in the BAL, nasal swabs, and throat swabs (Fig. 3F). Viral RNA from BAL and nasal swabs was positively correlated with IFN-activated monocytes, macrophages, and T cells in the BAL. In contrast, *PGTS2*$^+$ monocytes and naïve CD8$^+$ T cells from PBMCs negatively correlated with viral RNA from nasal swabs and BAL. To ask if type I, II, or III IFN was the stimulus for the IFN gene signature observed in many cell subsets, we analyzed *IFNB1*, *IFNG*, and *IFNL1* gene expression across all cell types (Fig. 3G). We found that *IFNB1* was up-regulated at day 4 post-infection, the timepoint when IFN-activated immune cells were highest. Interestingly, *IFNG* and *IFNFL1* showed a relative increase at day 10, when viral RNA had already decreased substantially. Across all cell types the most highly up-regulated, statistically significant IFN-stimulated genes were those downstream of type I IFN signaling and showed a pattern of up-regulation at day 4 post-infection. Together, these data indicated that SARS-CoV-2 infection induces a robust type I IFN-activated myeloid cell response in PBMC and BAL, which coincides with radiographic indications of inflammation and resolves along with viral RNA levels between day 7 to 10 post-infection.

Early B cell responses to SARS-CoV-2 infection

We measured multiple B cell subsets in PBMCs and BAL by flow cytometry, including resting naïve B cells (CD20$^+$IgD$^+$CD95$^-$), activated naïve B cells (CD20$^+$IgD$^+$CD95$^+$), germinal center B cells (GC B cells: CD20$^+$IgD$^-$BCL6$^+$Ki67$^+$), plasmablasts (CD20$^+$IgD-BCL-6$^-$CD38^{hi}CD27$^+$), and activated memory B cells (CD20$^+$IgD$^-$BCL-6$^-$CD95$^+$) (Figs S3A-B). Activated memory B cells were further subdivided into IgM$^+$, IgG$^+$, IgA$^+$, and isotype undefined. After infection, we observed a decrease in total B cells in PBMCs (Fig S3C), an increase of 2-3% in the proportion of activated naïve B cells from PBMC at day 4 and 7 (Fig S3D), and a decrease in the overall proportion of activated B cells in PBMCs that are isotype undefined (Fig S3E). At necropsy, the frequency of B cells varied across tissues. While the spleen had the largest fraction of B cells, the BAL and lung had the highest proportion of activated memory B cells (Fig S3D-H). Anti-spike IgM and IgG were first detectable in the plasma and BAL at ~day 10 post-infection in most animals, although levels were low compared to positive controls (~2-5 fold above background) (Fig S4). Low levels of neutralizing antibodies against SARS-

CoV-2/USA-WA1 were also detected in the plasma on day 10. Overall, there were very few changes in B cell populations over the first 10 days of infection, and antibody responses were just developing on day 10 post-infection.

Kinetics of SARS-CoV-2-specific effector CD8⁺ and CD4⁺ T cell responses in the BAL and PBMC

We next performed a flow cytometric analysis of the Ag-specific T cell response to SARS-CoV-2. We observed only minor changes in the activation of bulk T cell responses in the PBMC after infection, with more dynamic changes in the BAL after infection (Fig S5A-B). To examine SARS-CoV-2-specific T cell responses, we performed intracellular cytokine staining after ex vivo restimulation with peptide pools from the viral spike (S), nucleocapsid (N), and membrane (M) proteins, as well as peptide pools (megapools) derived from multiple SARS-CoV-2 antigens found to be immunogenic in humans (*68*, *69*). As expected, Ag-specific T cell responses were not detected at day 4 post-infection in PBMCs or BAL (Fig. 4A-D). CD4⁺ T cell responses to S, N, and megapool, each reached ~4-6% on average by day 7, whereas Ag-specific CD8⁺ T cells were ~1% at this timepoint in the BAL (Fig. 4B,D). Consistent with a slightly delayed response, Ag-specific CD8⁺ T cells in the BAL continued to expand in frequency and maintained Ki67 expression between days 7 and 10 post-infection, while Ag-specific CD4⁺ T cells peaked in frequency at day 7 and decreased Ki67 expression between days 7 and 10 (Fig. 4D-E). Of note, frequencies of Ag-specific T cells were ~10 to 20-fold higher in the BAL vs. PBMC. Moreover, CD8⁺ and CD4⁺ T cell responses against S and N were consistently immunodominant in comparison to M-specific T cells.

In addition to producing IFN$_\gamma$ and TNF after peptide stimulation, the majority of Ag-specific CD8⁺ T cells in the BAL also expressed granzyme B and degranulated after restimulation, as indicated by CD107a/b surface staining (Fig. 4F). Approximately 25-60% of Ag-specific CD4⁺ T cells in the BAL also made IL-2. Furthermore, both CD8⁺ and CD4⁺ Ag-specific T cells in the BAL up-regulated markers of tissue residence, CD69 and CD103, between days 7 and 10 post-infection (Fig S5C-D). Thus, SARS-CoV-2-specific CD8⁺ and CD4⁺ T cells in the airways displayed typical effector functions associated with cytotoxic T lymphocyte (CTL) and Th1 cells, respectively.

Distribution of SARS-CoV-2-specific CD8⁺ and CD4⁺ T cell responses in mucosal tissues

At the day 10 necropsy, we examined SLO and NLT from the upper and lower respiratory tract for bulk and Ag-specific T cells. Tissue resident memory CD8⁺ and CD4⁺ T cells (CD95⁺CD69⁺CD103$^{+/-}$) were detected in all nonlymphoid tissues measured, including the lung, nasal turbinates, salivary glands, and tonsils (Fig. 5A-B). CD103⁺ Trm were more abundant among CD8⁺ compared to CD4⁺ T cells in the BAL, salivary glands, and lymph nodes, which has been shown in other model systems (*70*, *71*). Using intravenous (i.v.) antibody staining to distinguish between tissue parenchymal and intravascular cells (*72–74*), we confirmed that most cells in the BAL, nasal turbinates, salivary gland, tonsils, and lymph nodes were from the tissue parenchyma (Fig S6). As expected for such a highly vascularized tissue, most cells from the lung were intravascular stain positive, but a small population of CD69⁺iv$^-$ cells were detectable in the lungs confirming that tissue resident cells were also detected in pulmonary tissue. We next quantified the magnitude of SARS-CoV-2-specific T cells in each of these tissues. S, N, and megapool-specific CD8⁺ and CD4⁺ T cells were detected in the BAL, previously PET hot lung lesions, pulmonary lymph nodes, peripheral lymph nodes, spleen, and PBMC (i.e., the frequency of IFN$_\gamma$⁺ and/or TNF⁺ cells after peptide restimulation was statistically significantly higher than the unstimulated samples). Surprisingly, Ag-specific CD8⁺ and CD4⁺ T cell responses could not be detected in the majority of nasal turbinates, salivary gland, and tonsils (Fig. 5C). The absence of Ag-specific T cells cannot be accounted for by poor T cell isolation from tissues (Fig. 5A-B) or lack of virus replication at these sites (Fig. 1D-F). Thus, the early clonal burst of SARS-CoV-2-specific T cells is highly focused on the BAL and unexpectedly undetectable in the nasal and oral mucosa.

Overall, the kinetics of SARS-CoV-2 replication and innate/adaptive immune response in rhesus macaques appears typical of an acute viral infection (Fig. 5D). SARS-CoV-2 replication peaks within 1 to 2 days post-infection and rapidly decreases thereafter. IFN-responsive myeloid responses are rapidly detected in the PBMC and BAL at day 4 post-infection. IFN-driven innate immune responses and lung inflammation then decline by day 7 post-infection, followed by an increase in inflammatory DCs and Ag-specific T cells at day 10.

DISCUSSION

We show here that during mild COVID-19 in rhesus macaques, SARS-CoV-2 replication is largely suppressed prior to the induction of virus-specific T cell responses. PET/CT imaging showed regions of ground glass opacity and consolidation with elevated ^{18}FDG uptake in the lungs on day 3 after SARS-CoV-2 infection, which completely resolved by day 9. A longitudinal scRNAseq analysis identified early type I IFN-responsive monocyte, macrophage, and dendritic cells in PBMC and BAL that mostly dissipated prior to the arrival of virus-specific CD8⁺ and CD4⁺ T cells. SARS-CoV-2-specific effector T cells were abundant in the pulmonary compartment, but undetectable in nasal turbinates, tonsils, and salivary glands, highlighting major differences in the localization of antigen-specific T cells in pulmonary and extrapulmonary mucosal tissues during SARS-CoV-2 infection.

Type I IFN is emerging as a critical mediator of control of SARS-CoV-2 infection (*4–6*). Type I IFN likely acts directly on

infected epithelial cells to suppress viral replication, but it may also be important in driving the activation of antiviral responses by myeloid cells. On day 4 after infection there was a striking increase in two populations of IFN-activated myeloid cells in the BAL, one having monocyte-like features and the other more closely resembling alveolar macrophages, indicating that recruited monocytes and lung resident macrophages are key early responders to type I IFN after SARS-CoV-2 infection. In our study, the abundance of type I IFN-activated myeloid cells in the BAL positively correlated with viral loads in the nasal swabs and BAL. These results are consistent with data from African green monkeys showing a strong type I IFN gene signature in macrophages from lung tissue three days after SARS-CoV-2 infection (*48*). However, several scRNAseq studies from patients with COVID-19 have found that inflammatory monocytes/macrophage populations are increased with disease severity (*3*, *10*, *12*, *14*), suggesting that early type I IFN responses are host-protective, but prolonged activation of this pathway may be detrimental. Consistent with this hypothesis, in this model of mild disease, we observed a rapid resolution of IFN-activated phagocytes in both the blood and BAL by day 7 post-infection.

On day 10 post-infection we observed a major reduction in the frequency of alveolar macrophages, which has also been documented in individuals with severe COVID-19 (*12*, *75*). Our data indicate that loss of alveolar macrophages can also occur after mild SARS-CoV-2 infection, so their loss may not be directly related to disease outcome. We also observed a major increase in the proportion of CD1c$^+$ dendritic cells in the BAL on day 10 post-infection, a time when Ag-specific T cells were abundant in the airways. Interestingly, CD1c$^+$ DCs displayed a distinct gene expression profile on day 10 with a notable increase in IL-1β and multiple pro-inflammatory chemokines. These cells may correspond to a population of inflammatory cDC2 that have been shown to appear in the lung after viral infection in mice (*76*). Notably, these cells were found to have an enhanced ability to stimulate both virus-specific CD4$^+$ and CD8$^+$ T cells. Collectively, our data indicate there may be two distinct phases of cellular innate immune responses in the BAL after SARS-CoV-2 infection. The first is characterized by an early wave of type I IFN-activated phagocytes, which may play an important role in the initial suppression of viral replication. The second is characterized by an abundance of pro-inflammatory dendritic cells, which may be key stimulators of the Ag-specific T cells that simultaneously arrive in the airways.

Ag-specific T cell responses were substantially greater in the BAL versus PBMCs, with the average sum of spike, nucleocapsid, and membrane-specific T cells reaching ~12% of CD4$^+$ T cells and ~7% of CD8$^+$ T cells in the BAL compared to ~1% and ~0.2% in PBMC, respectively. In the BAL, virus-specific Th1 cell responses preceded CTL responses. Indeed, the CD8$^+$ T cell clonal burst likely had not yet peaked, evidenced by their maintained expression of Ki67 at day 10 post-infection. The lack of virus-specific T cells in the nasal turbinates, salivary glands, and tonsils, despite virus infection and subsequent clearance from these tissues, was surprising. The mechanisms underlying the lack of antigen-specific effector T cells in the infected nasal and oral mucosa are not clear. It remains possible that SARS-CoV-2-specific T cell responses were not detected in these sites because they produce molecules other than IFN$_\gamma$, TNF, IL-2, granzyme B, or degranulation markers CD107a/b, after ex vivo peptide stimulation (i.e., Th2 cytokines, which were not measured here). Alternative techniques for functionally agnostic detection of SARS-CoV-2-specific T cell responses, such as the activation induced marker (AIM) assay, should be tested in future studies (*17*, *69*, *77*). Nevertheless, it is unlikely that T cells in the nasal turbinates, salivary glands, and tonsils have a completely different functional profile compared to their counterparts in the rest of the host. There may also be T cells in these tissues specific to antigens other than the ones tested here, although this too seems unlikely, as the peptide pools used contain numerous immunogenic peptides from across the entire viral genome (*68*). Lastly, it is possible that T cells accumulate in these tissues after day 10, and further studies will be needed to determine the longevity and breadth of SARS-CoV-2-specific T cell responses in tissues at later time points. The paucity of SARS-CoV-2-specific T cells in the nasal and oral mucosa may at least partly explain the observation of individuals previously infected with SARS-CoV-2 becoming re-infected (*78*–*80*).

Our findings support the hypothesis that control of primary SARS-CoV-2 infection in these tissues is largely T cell-independent, which is consistent with a recent report showing that rhesus macaques depleted of CD4- and/or CD8α-expressing cells prior to SARS-CoV-2 infection controlled the virus in the upper and lower respiratory tract, albeit perhaps with a slight delay (*64*). Another study also found that CD8 depletion in cynomolgus macaques had no impact on control of SARS-CoV-2 infection (*81*). It is important to point out, however, that our data do not rule out a critical role for T cells in other settings of SARS-CoV-2 infection. For example, T cells likely play a significant role when SARS-CoV-2 infection does not resolve quickly, such as during moderate and severe COVID-19. T cells have been implicated in control of SARS-CoV-2 in other susceptible animal models, like the human ACE2-expressing mouse lines and Syrian hamsters (*82*–*84*). Furthermore, nucleocapsid-specific CD8$^+$ T cells are correlated with less severe disease in patients (*20*). In addition, preclinical studies suggest that depletion of CD8$^+$ T cells from vaccinated monkeys prior to SARS-CoV-2 challenge significantly impairs control of virus replication (*59*). T cells may also play a major role in vaccine-elicited protection, and T cell-targeted peptide vaccines are currently being developed

(*20*, *85*, *86*). Vaccine-elicited T cells may prove critical in protection against SARS-CoV-2 variants of concern that are able to evade neutralizing antibodies, as T cell epitopes are thought to be more conserved across isolates (*87–92*). It should also be noted that we cannot rule out the possibility that T cells may have played a role in clearance of any residual virus-infected cells remaining in the lungs after the first week, when T cells arrived in the tissue.

Altogether, these data show that mild SARS-CoV-2 infection is associated with effective innate immune-mediated control. Future studies are needed to determine the importance of individual innate and adaptive immune cell types in suppression of SARS-CoV-2 replication.

MATERIALS AND METHODS

Study design

The study was designed with the goal of assessing the differential kinetics of lung inflammation, viral replication, innate, and adaptive cellular immune responses against SARS-CoV-2 infection in a model of mild disease. The study had a predetermined end point of day 10 post-infection. The number of animals included in the study was based on previous experience in detecting immune responses in non-human primate infection studies, as well as practical limitations. The first 4 animals to be infected were selected for subsequent single cell RNA sequencing analysis.

Animals and infection

Six, male rhesus macaques aged 2.5 to 6 years, weighing 3-10 kg were infected with SARS-CoV-2/USA/WA-1 (Table S1). For infection, animals were anesthetized as described below and administered $2x10^6$ $TCID_{50}$ total of SARS-CoV-2/USA-WA-1: $1x10^6$ $TCID_{50}$ in 3mL intratracheally with a plastic gavage tube attached to 5 mL syringe, and $5x10^5$ $TCID_{50}$ in 0.5mL intranasally in each nostril. The animals were examined daily with a health scoring sheet, as previously described (*42*). Animals were anesthetized with ketamine and dexmedetomidine at pre-infection (day -4 to -55), day 0, 1, 2, 3, 4, 7, and 10 (necropsy) for exams, PET/CT scans, viral swabs, blood and BAL fluid draws, and analysis of complete blood count and C-reactive protein. During anesthesia, animals were weighed and monitored for heart rate, respiratory rate, body temperature, oxygen saturation. Glycopyrrolate and atipamezole were given for recovery from anesthesia. For each animal, the pre-infection/baseline PET/CT scans are as follows DGCX and DG3V: day -55, DHGF and DHKM: day -17, and DGRX and DG4i: day -26. The pre-infection timepoints for swabs, blood, and BAL are as follows DGCX and DG3V: day -4, DHGF and DHKM: day -14, and DGRX and DG4i: day -5. Graphs including data plotted longitudinally, any pre-infection timepoints were represented as day 0.

All animal experiments were approved by Animal Care and Use Committee (ACUC) and all methods were performed under animal safety protocol LPD-25E at the National Institute of Health. Experiments were conducted in an AAALAC accredited aBSL-3 vivarium facility. Animals were singly housed in vented air cages with a 12-hour light/dark cycle. The animals were monitored twice daily, with a detailed physical exam once per day during the study. The Institutional Biosafety Committee approved all work with SARS-CoV-2 in the BSL-3 level facility and approved any inactivation methods used.

^{18}FDG-PET/CT Acquisition and Data Analysis

Rhesus were sedated and imaged by PET/CT during mechanical ventilation (Hallowell Ventilator Model 2002) at baseline and on day 3, and 9 post-infection. To reveal metabolic hyperactivity consistent with inflammation, a [^{18}F]-FDG dose of 0.5 mCi/kg was given intravenously 1 hour prior to PET imaging. During the uptake time a high-resolution CT scan of the lungs was acquired with a breath hold on a LFER 150 PET/CT scanner (Mediso Inc, Budapest, Hungary) as previously described (*93*). The raw CT and PET data were reconstructed using the Nucline software (Mediso, Inc, Budapest, Hungary) to create individual DICOM files that were co-registered using MIM Maestro (v. 7.0, MIM Software Inc, Cleveland, Ohio).

By aligning baseline PET/CT fused images and those taken at day 3 and 9 in MIM Maestro, specific lung regions with abnormal density (> ~ -550 HU) or metabolic activity (> ~ 1.5 SUV) were identified as volumes of interest (VOI) or lesions similar to methods used previously, rather than using whole lung volume of interest (*94*). For each animal, the lesion VOIs (day 3 in this study) were transferred to the aligned PET/CT images acquired at baseline and the day 9 time point, adjusting for position variations but keeping the same volume. Disease volume was estimated by using two density thresholds: tissues harder than -550 Hounsfield Units (HU) or harder than -300 HU for evaluating change over time. Regarding metabolic activity, PET parameters were estimated using a threshold of > 2 standardized uptake value (SUV). Similar reference VOIs were used to identify metabolically activated tissues (SUV > 2) within peri-carinal lymph nodes (LN). LN [^{18}F]-FDG uptake was measured in activated regions of the hilar and subcarinal LNs of each animal. Our analysis also included calculations of total lesion glycolysis (TLG). Two readers independently performed image analysis for each animal using consistent lesion labeling determined by a third reviewer. Three-dimensional projections of FDG uptake in the lung regions were generated using Osirix v 5.9 software (Pixmeo, Geneva, Switzerland) as previously described (*95*).

Blood and BAL collection

Blood and BAL collection procedures followed ACUC approved standard operating procedures and limits. Blood was collected in EDTA tubes and centrifuged at 2,000rpm for 10 min at 22°C to isolate plasma. After plasma removal, remaining blood was diluted 1:1 with 1x PBS. 15mL of 90% Ficoll-

Paque density gradient (Cytiva Cat#17144002), diluted with 10x PBS, was added to SepMate PBMC Isolation Tubes (StemCell Cat#85450) and centrifuged at 1,000 g for 1 min at 22°C, to collect Ficoll below the separation filter. Blood and PBS mix was added to the SepMate tube with Ficoll-Paque and centrifuged at 1,200 g for 10 min at 22°C. The upper layer was poured into a 50mL conical and brought to 50mL with PBS +1% FBS, and then centrifuged at 1,600rpm for 5 min at 4°C. The cell pellet was resuspended at $2x10^7$ cell/mL in X-VIVO 15 media + 10% FBS for subsequent analysis. BAL was collected after intubation by instillation of 50mL of warm pharmaceutical-grade PBS, 10mLs at a time. For cellular analysis, BAL was filtered through a 100um filter into a 50mL conical and centrifuged at 1,600 rpm for 15 min at 4°C. The cell pellet was resuspended at $2x10^7$ cell/mL in X-VIVO 15 media + 10% FBS for subsequent analysis.

Necropsy

Intravenous antibody was administered prior to euthanasia, as previously described (*73*). Briefly, prior to necropsy, 10mL of blood was drawn as a negative control and 100ug/kg of αCD45-biotin (clone: ITS_rhCD45 developed by Roederer Lab) was infused. The infusion was circulated for 10 min prior to terminal exsanguination and necropsy. The BAL and another ~60mL of blood were collected during exsanguination. After prosection of the lung and airways, specific lung regions observed to have abnormal HU density or FDG uptake in the day 3 images were scan-matched and collected separately as follows. The PET/CT scan images from day 3 post-infection were used to locate the airway vascular bundle adjacent to the abnormality. At necropsy, the lung parenchyma was resected back to reveal the bronchus upstream of the abnormality, which was followed to the target region to be resected. We have used a similar technique for PET/CT scan matching at necropsy after *Mycobacterium tuberculoisis* infection (*96*). LNs identified as having regions of SUV > 2.5 were collected separately from those with lower SUV on day 3. Normal lung sections were taken from each lobe. The resected lung sections, nasal turbinates, salivary gland, tonsils, spleen, and lymph nodes along with were then divided for RNA isolation, histology, and flow cytometry analysis.

Viral RNA quantification

RNA from the nose and throat was collected by swabbing each nostril or back of the throat, respectively, with a sterile swab for 10 s. Swabs were placed in 1mL viral transport media (1x HBSS, 2% FBS, 100ug/mL Gentamicin, and 0.5ug/mL amphotericin B) and stored on ice until RNA extraction. Swabs were vortexed in swab media before removing the swab tip. For RNA extraction 140uL of sample (plasma, 1st BAL wash, or swab media) was processed using a Viral RNA mini kit (Qiagen Cat# 52906) and eluted in 50uL RNase Free water. For RNA isolation from tissues, tissue pieces were weighed before placing in 1mL RNAlater® media (Sigma Cat# R0901) and stored at 4°C overnight and then stored at -80°C long term. Tissues were then thawed and processed in the RNeasy Plus Mini kit (Qiagen # 74136) and eluted in 50uL RNase Free water. Eluted RNA was stored at -80°C long-term.

Extracted RNA was used in a RT-qPCR reaction for detection of total or subgenomic RNA from the N gene of SARS-CoV-2. Total RNA reactions amplify both genomic viral RNA and subgenomic viral mRNAs and are labeled as genomic throughout the manuscript to differentiate from the subgenomic viral mRNA-specific amplifications. Each sample was prepared in a 12.5uL reaction, with 2.5uL of eluted RNA, 3.25uL Taqpath 1-step RT-qPCR Master Mix (Thermo Cat#A15299), primers at 500nM, probes at 125-200nM, and the remaining volume as RNase free water. N1 genomic RNA was detected with 2019-nCoV RUO Kit, 500 rxn (IDT #10006713), containing CDC 2019-nCoV_N1 Forward Primer (5′-GAC CCC AAA ATC AGC GAA AT-3′), CDC 2019-nCoV_N1 Reverse Primer (5′-TCT GGT TAC TGC CAG TTG AAT CTG-3′), and CDC 2019-nCoV_N1 Probe (5′-[FAM]-ACC CCG CAT TAC GTT TGG TGG ACC-[BHQ1]-3′) at 125nM. N gene subgenomic RNA was detected using Forward Leader sequence primer (5′-CGA TCT CTT GTA GAT CTG TTC TC-3′), sgN Reverse (5′-GGT GAA CCA AGA CGC AGT AT-3′), and sgN Probe (5′-[FAM]-TAA CCA GAA TGG AGA ACG CAG TGG G-[BHQ1]-3′,) at 200nM, all custom made from Eurofins. All samples were tested for RNA integrity using the 2019-nCoV RUO Kit for RNase P, containing CDC RNAse P Forward Primer (5′-AGA TTT GGA CCT GCG AGC G-3′), CDC RNAse P Reverse Primer (5′-GAG CGG CTG TCT CCA CAA GT-3′), and CDC RNAse P Probe (5′-[FAM]-TTC TGA CCT GAA GGC TCT GCG CG-[BHQ]-1-3′). Prepared reactions were read on a QuantStudio 7 Flex Real-Time PCR System, 384-well format (Applied Biosystems Cat# 4485701). Cycling conditions: Initial: 25°C for 2 min, 50°C for 15 min, and 95°C for 2 min, Cycling: 95°C for 3 s, 60°C for 30 s, for 40 cycles. Copies per/mL or copies/gram were calculated based on standard curves generated for each RT-qPCR run, with RNA standard of known quantity and 10, 5-fold dilutions, run in duplicate. The limit of detection was based on the CT limit of detection from the standard curve in each run. For genomic RNA, this was also limited to CT<35, based on manufacturer's instructions. For subgenomic RNA cutoff CT<37 was used.

Tissue digestion

Tissues were processed for single cell suspension before flow cytometry or peptide stimulation as follows. Spleen (approximately 0.5 inch × 0.5 inch portion) and lymph nodes were placed in 5mL of PBS + 1% FBS in a gentleMACS C tube (Miltenyi Cat#130096334) and run on gentleMACS Octo Dissociator (Miltenyi), with m_spleen_02_01 setting, then filtered through a 100um filter into a 50mL conical and centrifuged at 1,600rpm for 5 min at 4°C. Salivary gland was gentleMACS dissociated as above, and after centrifugation

cells were resuspended in 7mL 44% Percoll® (Sigma Cat# P1644) with 1xPBS and centrifuged at 2,000rpm for 20 min at 22°C without brake. The tonsil and lung were gentleMACS dissociated in 5mL digestion buffer (RPMI + 50U/mL DNase I + 1mg/mL hyaluronidase + 1mg/mL collagenase D (Roche)) and then agitated on a shaker at 220rpm for 45 min at 37°C. Digestion reaction was stopped with equal parts PBS + 20% FBS and centrifuged at 1,600rpm for 5 min at 22°C. The cell pellet was resuspended in Percoll gradient, as above for salivary gland. After processing, the spleen and lung were cleared of red blood cells by resuspending cell pellet in 2mL of ACK Lysing Buffer (Quality Biologicals Cat#118-156-101) for 2 min at room temperature, then stopping the reaction with 10-20mL of PBS + 1%FBS. Cells were resuspended at $2x10^7$ cell/mL in X-VIVO 15 media + 10% FBS for further analysis.

Peptide stimulation assay

Single cell suspensions were plated at $2x10^7$ cell/mL in 200uL in 96 well plates with X-VIVO 15 media, plus 10% FBS, Brefeldin 1000x (Invitrogen Cat#00-4506-51) and Monensin 1000x (Invitrogen Cat#00-4505-51), CD107a APC 1:50, CD107b APC 1:50, and peptide pools at 1ug/mL. If cell counts from individual lung sections were below $5x10^5$ total cells, sections of similar kind were pooled together to reach the concentration for stimulation. Cells were then stimulated for 6 hours at 37°C + 5% CO_2 before surface staining. Spike peptide pool consisted of Peptivator SARS-CoV-2 Prot_S1 (Miltenyi Cat#130-127-048) and Peptivator SARS-CoV-2 Prot_S (Miltenyi Cat#130-127-953). Nucleocapsid peptide pool consisted of Peptivator SARS-CoV-2 Prot_N (Miltenyi Cat# 130-126-699). Membrane peptide pool consisted of Peptivator SARS-CoV-2 Prot_M (Miltenyi Cat# 130-126-703). CD4 megapool consisted of CD4_S_MP and CD4_R_MP, and CD8 megapool consisted of CD8_MP_A and CD8_MP_B, as described (*69*). After stimulation cells were centrifuged at 1,600 rpm for 5 min at 4°C and proceeded with surface staining. For enumeration of the frequency of antigen-specific populations responding each peptide pool, the frequency of $IFN\gamma^+$ or TNF^+ $CD4^+$ or $CD8^+$ T cells in each condition was adjusted for background staining in unstimulated wells (% stimulated - % unstimulated). For Fig. 4C-D, statistical analysis was done on frequencies of antigen-specific $CD4^+$ and $CD8^+$ T cells after background subtraction. In Fig. 5C the statistical analysis was a paired *t* test of frequencies of antigen-specific $CD4^+$ or $CD8^+$ T cells between stimulated and unstimulated samples, for reporting of the detection of antigen-specific populations above background in each tissue.

Flow cytometry and antibody staining

Cells were resuspended in 50uL surface stain antibodies diluted in PBS + 1% FBS and incubated for 20 min at 4°C. Cells were washed 3 times with PBS + 1% FBS, before fixation with eBioscience Intracellular Fixation & Permeabilization Buffer Set (Thermo Cat# 88-8824-00) for 16 hours at 4°C. After fixation cells were centrifuged at 2,200rpm for 5 min at 4°C without brake and washed once with eBioscience Permeabilization Buffer. Cells were resuspended in 50uL intracellular stains diluted in eBioscience Permeabilization Buffer, and stained for 30 min at 4°C. After staining cells were washed with eBioscience Permeabilization Buffer 2x and resuspended in PBS + 1% FBS + 0.05% Sodium Azide for running on the BD Symphony platform.

B cells were resuspended in 50uL Human Fc-Block (BD Cat#564220) diluted to1:500 in PBS + 1%FBS and incubated for 30 min at 4°C prior to washing and surface staining. Antibodies used can be found in Table S2. The biotinylated intravenous antibody was detected with Streptavidin conjugated to the indicated fluorophore included in the surface stain. The intravenous stain (i.v. stain) positive cells are localized to the tissue vasculature, while i.v. stain negative cells are localized to the tissue parenchyma. For phenotypic marker analysis of antigen-specific T populations, a cutoff of >35 peptide-specific T cells per samples was used for subsequent analysis to prevent the introduction of error from quantifying too few events.

Fluorescent ELISA

High-binding polystyrene half-area 96 well plates (Greiner Bio-One Cat#675077) were coated with recombinant SARS-CoV-2 Spike Trimer (Miltenyi Cat#130-127-683) at 2ug/mL and 25uL per well for at least 16 hours at 4°C. Plates were washed with Wash Buffer (PBS + 0.05% Tween-20) using an automatic plate washer (5x with 180uL). Plates were blocked with 25uL per well of Blocking Buffer (PBS + 1% BSA + 0.01% Tween-20) for at least 16 hours at 4°C. Plates were washed again as above. Plasma and BAL fluid were initially diluted 1:10 with Blocking Buffer and 3 -fold serial diluted for a total of 12 dilutions per sample. The dilutions were plated at 25uL per well and incubated for 1 hour at 37°C. Plates were washed again as above. Goat anti-monkey IgG-HRP (Invitrogen Cat#PA1-84631) and goat anti-monkey IgM-HRP (Alpha Diagnostics Cat#70031) were diluted with Blocking Buffer 1:3000 and 1:2000, respectively. Secondary antibodies were plated at 25uL per well and incubated 30 min at 37°C. Plates were washed again as above. Plates were developed with QuantaRed Enhanced Chemifluorescent HRP Substrate Kit (Thermo Cat#15159), following manufacturer's instructions for reagent preparation, and incubated for 15 min for IgG and 30 min for IgM, and the reaction was stopped with the manufacturer provided Stop Solution. Plates were immediately read on a SpectraMax Gemini fluorescent microplate reader (Molecular Devices) with Excitation of 570nm and Emission of 585nm.

Live-virus neutralization assay

Vero-E6 cells stably expressing human TMPRSS2 (Vero-E6T2) (*97*), a gift from the laboratory of Jonathan Yewdell (NIAID), were maintained at 37°C and 5% CO_2 in D10+

medium (DMEM +10% FBS, 1X Glutamax, 1X Anti-Anti (Gibco) and 250ug/mL Hygromycin B (InVivoGen)). One day before the assay, cells were plated in 12-well plates (Falcon Cat#353043) at a density of 0.4 million cells per well in 2mL D10+ medium. The day of the assay, 12-well plates were washed twice with D2 medium (DMEM + 2%FBS, 1X Glutamax).

Rhesus macaque plasma samples, collected at day 0 and day 10 post-infection with SARS-CoV-2, were heat inactivated at 56°C for 30 min. After an initial 1:5 dilution, plasma samples were further two-fold serially diluted with D2 medium and 100uL of each dilution was incubated for one hour at 37°C with an equivalent volume of D2 medium containing 40-50 PFU of SARS-CoV-2 USA-WA1/2020 virus. After the incubation, 100uL of plasma/virus mixture was added to Vero-E6T2 in duplicate wells containing 300uL of D2 medium. The virus was allowed to absorb onto the cells for one hour at 37°C and 5% CO_2 with occasional mixing. At the end of the incubation, 1.5mL of DMEM medium supplemented with 0.6% of methyl cellulose was added per well and the plates were maintained for another 66 to 72 hours at 37°C and 5% CO_2. At the end of the incubation, the medium was removed and replaced with 1mL of Crystal Violet solution containing 5% ethanol and 3% neutral buffered formamide. The wells were stained for 20 min at room temperature, then washed briefly with deionized water and air dried in the biosafety cabinet. Once dry, the plates were scanned at 300dpi and plaques were counted from the images. Percent of inhibition was calculated based on the number of plaques observed for each dilution compared to controls. The IC50 of the percent inhibition for the dilution series was calculated based on non-linear regression. Each experiment included the following controls: uninfected cells as negative control, virus in absence of rhesus macaque serum and virus incubated with a dilution of a known positive serum (kindly provided by SAB Biotherapeutics).

Immunohistochemistry and RNA scope

Tissue for histology were collected in 10% neutral buffered formalin and stored at room temperature for 16 hours. Fixed tissues were transferred to 70% ethanol and stored at room temperature until processing. Slides were cut 10-microns thick using standard RNAse precautions. Immunohistochemical slides were deparaffinized and treated with AR6 Buffer (Akoya Biosciencecs, USA) for 20 min at 100°C. Tissues were then permeabilized using 0.2% TritonX 100 (Millipore Sigma, USA) for 10 min. After blocking, slides were incubated with primary antibodies against CD62P (clone EPR22850-190, Abcam, USA) and fibrin (clone 59D8, Millipore Sigma, USA) at a 1:500 and 1:200 concentration, respectively. Following washing, slides were stained according to the protocol for ImmPRESS Duet Double Staining Polymer Kit (Vector Laboratories, USA) and counter-stained with hematoxylin. Slides used for in situ hybridization were deparaffinized and treated with RNAscope epitope retrieval buffer (ACD Biotechne, USA) for 20 min at 100°C. Endogenous peroxidases were then blocked with hydrogen peroxide and tissue permeabilized with a diluted RNAscope protease plus for 20 min at 40°C. Probes for SARS-CoV-2, containing 20 pairs of probes spanning S gene (Category # 848561, ACD Biotechne, USA), were incubated for 2 hours at 40°C. Slides were then processed according to RNAscope 2.5 HD Assay-RED (ACD Biotechne, USA) protocol and counterstained with hematoxylin. Slides stained immunohistochemically or by in situ hybridization were imaged using Aperio VERSA (Leica Microsystems, USA) and analyzed using quPath, an open-source software developed by the University of Edinburgh. SARS-CoV-2 puncta were confirmed using both positive and negative controls to ensure accurate staining.

Single cell RNA sequencing and data analyses

Cells from the BAL fluid and PBMCs from blood were obtained as described above and cryopreserved in 1ml of RPMI + 40% FBS + 15% DMSO. PBMC and BAL samples from days -7, 4, 7, 10 for monkeys DHGF, DG3V and DHKM and both sample types from days -7, 4 and 10 for monkey DGCX were processed for scRNAseq using the 10X Genomics Chromium Single Cell 3′ kit (v3.1). Briefly, cryopreserved samples were quickly thawed using a water bath set to 37°C and washed twice using 10% FBS in RPMI. Samples were then stained with unique TotalSeq-A hashtag antibodies (HTO) as per manufacturer's (Biolegend) protocol. Equal number of cells from each sample were pooled and super-loaded on a 10X Genomics Next GEM chip and single cell GEMs were generated on a 10X Chromium Controller as previously described (*98*). Subsequent steps to generate cDNA and HTO libraries were performed following 10X Genomics and Biolegend's protocol respectively. Libraries were pooled and sequenced on an Illumina NovaSeq S1 and S2 flow cells as per 10X sequencing recommendations.

The sequenced data was processed using cellranger (version 5.0) to demultiplex the libraries. The reads were aligned to *Macaca mulatta* mmul_10 genome to generate count tables. The count tables were then further processed and analyzed using the Seurat (version 4.0) in R (version 4.1.0). Samples from different PBMC and BAL libraries were integrated using IntegrateData function to account for possible batch effects and to generate one integrated dataset for each tissue type. Cells were then filtered for less than 15% mitochondrial contamination and only singlets as determined by the HTOs were included resulting in 16,769 PMBC and 7,274 BAL cells for downstream analysis. Data were normalized and scaled and FindVariableFeatures function was used to identify variable genes to subset and integrate the data to correct for animal bias. Principal component analysis was performed to find neighbors and clusters and UMAP reduction

was performed with 20 dimensions. FindAllMarkers with a filter of log fold change ≥ 0.25 and percent of cells expressing the marker ≥ 0.25 was used to identify gene markers that distinguish the cell clusters, and the clusters were manually assigned cell types based on identified canonical markers. Myeloid and T (and NK in case of PBMC) cell clusters were further subclustered and clusters were again manually annotated based on gene markers determined by the FindAllMarkers function. Differentially expressed genes between timepoints of a particular cluster were identified by running FindMarkers function with MAST and comparing one timepoint to all other timepoints or one timepoint to another in a pairwise manner. Genes with a log fold change ≥ 0.5, percent of cells expressing the marker ≥ 0.25 and adjusted p value ≤ 0.01 were considered significant and these genes were hierarchically clustered and displayed as a heatmap using the ComplexHeatmap function in R. Gene ontology enrichment analysis of genes up-regulated at a particular timepoint was performed using clusterProfiler to identify biological processes (adjusted p value ≤ 0.05). The AverageExpression function was used to calculate average gene expression of IFN and IFN-stimulated genes across all cells over time and was visualized using pheatmap.

Spearman's correlation test was performed between viral loads from various sites and fraction of cells in a particular cluster at all available timepoints and filtered for adjusted p value < 0.05. Correlations were visualized using a network diagram generated using igraph in R. Hashtag antibodies used can be found Table S2.

Statistical analysis

Data were analyzed using a two-way ANOVA with a Sidak's multiple comparison test, a Turkey's multiple comparison test, or a Dunnett's multiple comparison test; a one-way ANOVA using a Dunnett's multiple comparison test; or a two-tailed paired *t* test. Tests used are indicated in figure legends. For all statistical analysis p<0.05 for the given test is considered significant: * p<0.05, ** p<0.01, *** p<0.001, **** p<0.0001

SUPPLEMENTARY MATERIALS

www.science.org/doi/10.1126/sciimmunol.abo0535
Figs. S1 to S6
Tables S1 and S2
Data file S1

REFERENCES AND NOTES

1. G. Chen, D. Wu, W. Guo, Y. Cao, D. Huang, H. Wang, T. Wang, X. Zhang, H. Chen, H. Yu, X. Zhang, M. Zhang, S. Wu, J. Song, T. Chen, M. Han, S. Li, X. Luo, J. Zhao, Q. Ning, Clinical and immunological features of severe and moderate coronavirus disease 2019. *J. Clin. Invest.* **130**, 2620–2629 (2020). doi:10.1172/JCI137244 Medline
2. S. K. Dhar, V. K, S. Damodar, S. Gujar, M. Das, IL-6 and IL-10 as predictors of disease severity in COVID-19 patients: Results from meta-analysis and regression. *Heliyon* **7**, e06155 (2021). doi:10.1016/j.heliyon.2021.e06155 Medline
3. E. Stephenson, G. Reynolds, R. A. Botting, F. J. Calero-Nieto, M. D. Morgan, Z. K. Tuong, K. Bach, W. Sungnak, K. B. Worlock, M. Yoshida, N. Kumasaka, K. Kania, J. Engelbert, B. Olabi, J. S. Spegarova, N. K. Wilson, N. Mende, L. Jardine, L. C. S. Gardner, I. Goh, D. Horsfall, J. McGrath, S. Webb, M. W. Mather, R. G. H. Lindeboom, E. Dann, N. Huang, K. Polanski, E. Prigmore, F. Gothe, J. Scott, R. P. Payne, K. F. Baker, A. T. Hanrath, I. C. D. Schim van der Loeff, A. S. Barr, A. Sanchez-Gonzalez, L. Bergamaschi, F. Mescia, J. L. Barnes, E. Kilich, A. de Wilton, A. Saigal, A. Saleh, S. M. Janes, C. M. Smith, N. Gopee, C. Wilson, P. Coupland, J. M. Coxhead, V. Y. Kiselev, S. van Dongen, J. Bacardit, H. W. King, A. J. Rostron, A. J. Simpson, S. Hambleton, E. Laurenti, P. A. Lyons, K. B. Meyer, M. Z. Nikolić, C. J. A. Duncan, K. G. C. Smith, S. A. Teichmann, M. R. Clatworthy, J. C. Marioni, B. Göttgens, M. Haniffa; Cambridge Institute of Therapeutic Immunology and Infectious Disease-National Institute of Health Research (CITIID-NIHR) COVID-19 BioResource Collaboration, Single-cell multi-omics analysis of the immune response in COVID-19. *Nat. Med.* **27**, 904–916 (2021). doi:10.1038/s41591-021-01329-2 Medline
4. Q. Zhang, P. Bastard, Z. Liu, J. Le Pen, M. Moncada-Velez, J. Chen, M. Ogishi, I. K. D. Sabli, S. Hodeib, C. Korol, J. Rosain, K. Bilguvar, J. Ye, A. Bolze, B. Bigio, R. Yang, A. A. Arias, Q. Zhou, Y. Zhang, F. Onodi, S. Korniotis, L. Karpf, Q. Philippot, M. Chbihi, L. Bonnet-Madin, K. Dorgham, N. Smith, W. M. Schneider, B. S. Razooky, H. H. Hoffmann, E. Michailidis, L. Moens, J. E. Han, L. Lorenzo, L. Bizien, P. Meade, A. L. Neehus, A. C. Ugurbil, A. Corneau, G. Kerner, P. Zhang, F. Rapaport, Y. Seeleuthner, J. Manry, C. Masson, Y. Schmitt, A. Schlüter, T. Le Voyer, T. Khan, J. Li, J. Fellay, L. Roussel, M. Shahrooei, M. F. Alosaimi, D. Mansouri, H. Al-Saud, F. Al-Mulla, F. Almourfi, S. Z. Al-Muhsen, F. Alsohime, S. Al Turki, R. Hasanato, D. van de Beek, A. Biondi, L. R. Bettini, M. D'Angio', P. Bonfanti, L. Imberti, A. Sottini, S. Paghera, E. Quiros-Roldan, C. Rossi, A. J. Oler, M. F. Tompkins, C. Alba, I. Vandernoot, J. C. Goffard, G. Smits, I. Migeotte, F. Haerynck, P. Soler-Palacin, A. Martin-Nalda, R. Colobran, P. E. Morange, S. Keles, F. Çölkesen, T. Ozcelik, K. K. Yasar, S. Senoglu, S. N. Karabela, C. Rodríguez-Gallego, G. Novelli, S. Hraiech, Y. Tandjaoui-Lambiotte, X. Duval, C. Laouénan, A. L. Snow, C. L. Dalgard, J. D. Milner, D. C. Vinh, T. H. Mogensen, N. Marr, A. N. Spaan, B. Boisson, S. Boisson-Dupuis, J. Bustamante, A. Puel, M. J. Ciancanelli, I. Meyts, T. Maniatis, V. Soumelis, A. Amara, M. Nussenzweig, A. García-Sastre, F. Krammer, A. Pujol, D. Duffy, R. P. Lifton, S. Y. Zhang, G. Gorochov, V. Béziat, E. Jouanguy, V. Sancho-Shimizu, C. M. Rice, L. Abel, L. D. Notarangelo, A. Cobat, H. C. Su, J. L. Casanova; COVID-STORM Clinicians; COVID Clinicians; Imagine COVID Group; French COVID Cohort Study Group; CoV-Contact Cohort; Amsterdam UMC Covid-19 Biobank; COVID Human Genetic Effort; NIAID-USUHS/TAGC COVID Immunity Group, Inborn errors of type I IFN immunity in patients with life-threatening COVID-19. *Science* **370**, eabd4570 (2020). doi:10.1126/science.abd4570 Medline
5. P. Bastard, L. B. Rosen, Q. Zhang, E. Michailidis, H. H. Hoffmann, Y. Zhang, K. Dorgham, Q. Philippot, J. Rosain, V. Béziat, J. Manry, E. Shaw, L. Haljasmägi, P. Peterson, L. Lorenzo, L. Bizien, S. Trouillet-Assant, K. Dobbs, A. A. de Jesus, A. Belot, A. Kallaste, E. Catherinot, Y. Tandjaoui-Lambiotte, J. Le Pen, G. Kerner, B. Bigio, Y. Seeleuthner, R. Yang, A. Bolze, A. N. Spaan, O. M. Delmonte, M. S. Abers, A. Aiuti, G. Casari, V. Lampasona, L. Piemonti, F. Ciceri, K. Bilguvar, R. P. Lifton, M. Vasse, D. M. Smadja, M. Migaud, J. Hadjadj, B. Terrier, D. Duffy, L. Quintana-Murci, D. van de Beek, L. Roussel, D. C. Vinh, S. G. Tangye, F. Haerynck, D. Dalmau, J. Martinez-Picado, P. Brodin, M. C. Nussenzweig, S. Boisson-Dupuis, C. Rodríguez-Gallego, G. Vogt, T. H. Mogensen, A. J. Oler, J. Gu, P. D. Burbelo, J. I. Cohen, A. Biondi, L. R. Bettini, M. D'Angio, P. Bonfanti, P. Rossignol, J. Mayaux, F. Rieux-Laucat, E. S. Husebye, F. Fusco, M. V. Ursini, L. Imberti, A. Sottini, S. Paghera, E. Quiros-Roldan, C. Rossi, R. Castagnoli, D. Montagna, A. Licari, G. L. Marseglia, X. Duval, J. Ghosn, J. S. Tsang, R. Goldbach-Mansky, K. Kisand, M. S. Lionakis, A. Puel, S. Y. Zhang, S. M. Holland, G. Gorochov, E. Jouanguy, C. M. Rice, A. Cobat, L. D. Notarangelo, L. Abel, H. C. Su, J. L. Casanova; HGID Lab; NIAID-USUHS Immune Response to COVID Group; COVID Clinicians; COVID-STORM Clinicians; Imagine COVID Group; French COVID Cohort Study Group; Milieu Intérieur Consortium; CoV-Contact Cohort; Amsterdam UMC Covid-19 Biobank; COVID Human Genetic Effort, Autoantibodies against type I IFNs in patients with life-threatening COVID-19. *Science* **370**, eabd4585 (2020). doi:10.1126/science.abd4585 Medline
6. J. Hadjadj, N. Yatim, L. Barnabei, A. Corneau, J. Boussier, N. Smith, H. Péré, B. Charbit, V. Bondet, C. Chenevier-Gobeaux, P. Breillat, N. Carlier, R. Gauzit, C. Morbieu, F. Pène, N. Marin, N. Roche, T. A. Szwebel, S. H. Merkling, J. M. Treluyer, D. Veyer, L. Mouthon, C. Blanc, P. L. Tharaux, F. Rozenberg, A. Fischer, D. Duffy, F. Rieux-Laucat, S. Kernéis, B. Terrier, Impaired type I interferon activity and

inflammatory responses in severe COVID-19 patients. *Science* **369**, 718–724 (2020). doi:10.1126/science.abc6027 Medline
7. T. S. Rodrigues, K. S. G. de Sá, A. Y. Ishimoto, A. Becerra, S. Oliveira, L. Almeida, A. V. Gonçalves, D. B. Perucello, W. A. Andrade, R. Castro, F. P. Veras, J. E. Toller-Kawahisa, D. C. Nascimento, M. H. F. de Lima, C. M. S. Silva, D. B. Caetite, R. B. Martins, I. A. Castro, M. C. Pontelli, F. C. de Barros, N. B. do Amaral, M. C. Giannini, L. P. Bonjorno, M. I. F. Lopes, R. C. Santana, F. C. Vilar, M. Auxiliadora-Martins, R. Luppino-Assad, S. C. L. de Almeida, F. R. de Oliveira, S. S. Batah, L. Siyuan, M. N. Benatti, T. M. Cunha, J. C. Alves-Filho, F. Q. Cunha, L. D. Cunha, F. G. Frantz, T. Kohlsdorf, A. T. Fabro, E. Arruda, R. D. R. de Oliveira, P. Louzada-Junior, D. S. Zamboni, Inflammasomes are activated in response to SARS-CoV-2 infection and are associated with COVID-19 severity in patients. *J. Exp. Med.* **218**, e20201707 (2021). doi:10.1084/jem.20201707 Medline
8. S. Sinha, N. L. Rosin, R. Arora, E. Labit, A. Jaffer, L. Cao, R. Farias, A. P. Nguyen, L. G. N. de Almeida, A. Dufour, A. Bromley, B. McDonald, M. R. Gillrie, M. J. Fritzler, B. G. Yipp, J. Biernaskie, Dexamethasone modulates immature neutrophils and interferon programming in severe COVID-19. *Nat. Med.* (2021). Medline
9. F. A. Lagunas-Rangel, Neutrophil-to-lymphocyte ratio and lymphocyte-to-C-reactive protein ratio in patients with severe coronavirus disease 2019 (COVID-19): A meta-analysis. *J. Med. Virol.* **92**, 1733–1734 (2020). doi:10.1002/jmv.25819 Medline
10. J. Schulte-Schrepping, N. Reusch, D. Paclik, K. Baßler, S. Schlickeiser, B. Zhang, B. Krämer, T. Krammer, S. Brumhard, L. Bonaguro, E. De Domenico, D. Wendisch, M. Grasshoff, T. S. Kapellos, M. Beckstette, T. Pecht, A. Saglam, O. Dietrich, H. E. Mei, A. R. Schulz, C. Conrad, D. Kunkel, E. Vafadarnejad, C. J. Xu, A. Horne, M. Herbert, A. Drews, C. Thibeault, M. Pfeiffer, S. Hippenstiel, A. Hocke, H. Müller-Redetzky, K. M. Heim, F. Machleidt, A. Uhrig, L. Bosquillon de Jarcy, L. Jürgens, M. Stegemann, C. R. Glösenkamp, H. D. Volk, C. Goffinet, M. Landthaler, E. Wyler, P. Georg, M. Schneider, C. Dang-Heine, N. Neuwinger, K. Kappert, R. Tauber, V. Corman, J. Raabe, K. M. Kaiser, M. T. Vinh, G. Rieke, C. Meisel, T. Ulas, M. Becker, R. Geffers, M. Witzenrath, C. Drosten, N. Suttorp, C. von Kalle, F. Kurth, K. Händler, J. L. Schultze, A. C. Aschenbrenner, Y. Li, J. Nattermann, B. Sawitzki, A. E. Saliba, L. E. Sander; Deutsche COVID-19 OMICS Initiative (DeCOI), Severe COVID-19 Is Marked by a Dysregulated Myeloid Cell Compartment. *Cell* **182**, 1419–1440.e23 (2020). doi:10.1016/j.cell.2020.08.001 Medline
11. E. R. Mann, M. Menon, S. B. Knight, J. E. Konkel, C. Jagger, T. N. Shaw, S. Krishnan, M. Rattray, A. Ustianowski, N. D. Bakerly, P. Dark, G. Lord, A. Simpson, T. Felton, L. P. Ho, M. Feldmann, J. R. Grainger, T. Hussell; NIHR Respiratory TRC; CIRCO, Longitudinal immune profiling reveals key myeloid signatures associated with COVID-19. *Sci. Immunol.* **5**, eabd6197 (2020). doi:10.1126/sciimmunol.abd6197 Medline
12. M. Liao, Y. Liu, J. Yuan, Y. Wen, G. Xu, J. Zhao, L. Cheng, J. Li, X. Wang, F. Wang, L. Liu, I. Amit, S. Zhang, Z. Zhang, Single-cell landscape of bronchoalveolar immune cells in patients with COVID-19. *Nat. Med.* **26**, 842–844 (2020). doi:10.1038/s41591-020-0901-9 Medline
13. E. J. Giamarellos-Bourboulis, M. G. Netea, N. Rovina, K. Akinosoglou, A. Antoniadou, N. Antonakos, G. Damoraki, T. Gkavogianni, M. E. Adami, P. Katsaounou, M. Ntaganou, M. Kyriakopoulou, G. Dimopoulos, I. Koutsodimitropoulos, D. Velissaris, P. Koufargyris, A. Karageorgos, K. Katrini, V. Lekakis, M. Lupse, A. Kotsaki, G. Renieris, D. Theodoulou, V. Panou, E. Koukaki, N. Koulouris, C. Gogos, A. Koutsoukou, Complex Immune Dysregulation in COVID-19 Patients with Severe Respiratory Failure. *Cell Host Microbe* **27**, 992–1000.e3 (2020). doi:10.1016/j.chom.2020.04.009 Medline
14. P. A. Szabo, P. Dogra, J. I. Gray, S. B. Wells, T. J. Connors, S. P. Weisberg, I. Krupska, R. Matsumoto, M. M. L. Poon, E. Idzikowski, S. E. Morris, C. Pasin, A. J. Yates, A. Ku, M. Chait, J. Davis-Porada, X. V. Guo, J. Zhou, M. Steinle, S. Mackay, A. Saqi, M. R. Baldwin, P. A. Sims, D. L. Farber, Longitudinal profiling of respiratory and systemic immune responses reveals myeloid cell-driven lung inflammation in severe COVID-19. *Immunity* **54**, 797–814.e6 (2021). doi:10.1016/j.immuni.2021.03.005 Medline
15. D. Mathew, J. R. Giles, A. E. Baxter, D. A. Oldridge, A. R. Greenplate, J. E. Wu, C. Alanio, L. Kuri-Cervantes, M. B. Pampena, K. D'Andrea, S. Manne, Z. Chen, Y. J. Huang, J. P. Reilly, A. R. Weisman, C. A. G. Ittner, O. Kuthuru, J. Dougherty, K. Nzingha, N. Han, J. Kim, A. Pattekar, E. C. Goodwin, E. M. Anderson, M. E. Weirick, S. Gouma, C. P. Arevalo, M. J. Bolton, F. Chen, S. F. Lacey, H. Ramage, S. Cherry, S. E. Hensley, S. A. Apostolidis, A. C. Huang, L. A. Vella, M. R. Betts, N. J. Meyer, E. J. Wherry; UPenn COVID Processing Unit, Deep immune profiling of COVID-19 patients reveals distinct immunotypes with therapeutic implications. *Science* **369**, eabc8511 (2020). doi:10.1126/science.abc8511 Medline
16. C. Lucas, P. Wong, J. Klein, T. B. R. Castro, J. Silva, M. Sundaram, M. K. Ellingson, T. Mao, J. E. Oh, B. Israelow, T. Takahashi, M. Tokuyama, P. Lu, A. Venkataraman, A. Park, S. Mohanty, H. Wang, A. L. Wyllie, C. B. F. Vogels, R. Earnest, S. Lapidus, I. M. Ott, A. J. Moore, M. C. Muenker, J. B. Fournier, M. Campbell, C. D. Odio, A. Casanovas-Massana, R. Herbst, A. C. Shaw, R. Medzhitov, W. L. Schulz, N. D. Grubaugh, C. Dela Cruz, S. Farhadian, A. I. Ko, S. B. Omer, A. Iwasaki; Yale IMPACT Team, Longitudinal analyses reveal immunological misfiring in severe COVID-19. *Nature* **584**, 463–469 (2020). doi:10.1038/s41586-020-2588-y Medline
17. C. Rydyznski Moderbacher, S. I. Ramirez, J. M. Dan, A. Grifoni, K. M. Hastie, D. Weiskopf, S. Belanger, R. K. Abbott, C. Kim, J. Choi, Y. Kato, E. G. Crotty, C. Kim, S. A. Rawlings, J. Mateus, L. P. V. Tse, A. Frazier, R. Baric, B. Peters, J. Greenbaum, E. Ollmann Saphire, D. M. Smith, A. Sette, S. Crotty, Antigen-Specific Adaptive Immunity to SARS-CoV-2 in Acute COVID-19 and Associations with Age and Disease Severity. *Cell* **183**, 996–1012.e19 (2020). doi:10.1016/j.cell.2020.09.038 Medline
18. J. Neidleman, X. Luo, A. F. George, M. McGregor, J. Yang, C. Yun, V. Murray, G. Gill, W. C. Greene, J. Vasquez, S. A. Lee, E. Ghosn, K. L. Lynch, N. R. Roan, Distinctive features of SARS-CoV-2-specific T cells predict recovery from severe COVID-19. *Cell Rep.* **36**, 109414 (2021). doi:10.1016/j.celrep.2021.109414 Medline
19. V. Mallajosyula, C. Ganjavi, S. Chakraborty, A. M. McSween, A. J. Pavlovitch-Bedzyk, J. Wilhelmy, A. Nau, M. Manohar, K. C. Nadeau, M. M. Davis, CD8$^+$ T cells specific for conserved coronavirus epitopes correlate with milder disease in COVID-19 patients. *Sci. Immunol.* **6**, eabg5669 (2021). doi:10.1126/sciimmunol.abg5669 Medline
20. Y. Peng, S. L. Felce, D. Dong, F. Penkava, A. J. Mentzer, X. Yao, G. Liu, Z. Yin, J. L. Chen, Y. Lu, D. Wellington, P. A. C. Wing, D. C. C. Dominey-Foy, C. Jin, W. Wang, M. A. Hamid, R. A. Fernandes, B. Wang, A. Fries, X. Zhuang, N. Ashley, T. Rostron, C. Waugh, P. Sopp, P. Hublitz, R. Beveridge, T. K. Tan, C. Dold, A. J. Kwok, C. Rich-Griffin, W. Dejnirattisa, C. Liu, P. Kurupati, I. Nassiri, R. A. Watson, O. Tong, C. A. Taylor, P. Kumar Sharma, B. Sun, F. Curion, S. Revale, L. C. Garner, K. Jansen, R. C. Ferreira, M. Attar, J. W. Fry, R. A. Russell, C. Consortium, H. J. Stauss, W. James, A. Townsend, L. P. Ho, P. Klenerman, J. Mongkolsapaya, G. R. Screaton, C. Dendrou, S. N. Sansom, R. Bashford-Rogers, B. Chain, G. L. Smith, J. A. McKeating, B. P. Fairfax, P. Bowness, A. J. McMichael, G. Ogg, J. C. Knight, T. Dong, An immunodominant NP105-113-B*07:02 cytotoxic T cell response controls viral replication and is associated with less severe COVID-19 disease. *Nat. Immunol.* (2021). Medline
21. D. S. Khoury, D. Cromer, A. Reynaldi, T. E. Schlub, A. K. Wheatley, J. A. Juno, K. Subbarao, S. J. Kent, J. A. Triccas, M. P. Davenport, Neutralizing antibody levels are highly predictive of immune protection from symptomatic SARS-CoV-2 infection. *Nat. Med.* **27**, 1205–1211 (2021). doi:10.1038/s41591-021-01377-8 Medline
22. K. A. Earle, D. M. Ambrosino, A. Fiore-Gartland, D. Goldblatt, P. B. Gilbert, G. R. Siber, P. Dull, S. A. Plotkin, Evidence for antibody as a protective correlate for COVID-19 vaccines. *Vaccine* **39**, 4423–4428 (2021). doi:10.1016/j.vaccine.2021.05.063 Medline
23. S. Feng, D. J. Phillips, T. White, H. Sayal, P. K. Aley, S. Bibi, C. Dold, M. Fuskova, S. C. Gilbert, I. Hirsch, H. E. Humphries, B. Jepson, E. J. Kelly, E. Plested, K. Shoemaker, K. M. Thomas, J. Vekemans, T. L. Villafana, T. Lambe, A. J. Pollard, M. Voysey; Oxford COVID Vaccine Trial Group, Correlates of protection against symptomatic and asymptomatic SARS-CoV-2 infection. *Nat. Med.* **27**, 2032–2040 (2021). doi:10.1038/s41591-021-01540-1 Medline
24. V. J. Hall, S. Foulkes, A. Charlett, A. Atti, E. J. M. Monk, R. Simmons, E. Wellington, M. J. Cole, A. Saei, B. Oguti, K. Munro, S. Wallace, P. D. Kirwan, M. Shrotri, A. Vusirikala, S. Rokadiya, M. Kall, M. Zambon, M. Ramsay, T. Brooks, C. S. Brown, M. A. Chand, S. Hopkins; SIREN Study Group, SARS-CoV-2 infection rates of antibody-positive compared with antibody-negative health-care workers in England: A large, multicentre, prospective cohort study (SIREN). *Lancet* **397**, 1459–1469 (2021). doi:10.1016/S0140-6736(21)00675-9 Medline
25. M. M. L. Poon, K. Rybkina, Y. Kato, M. Kubota, R. Matsumoto, N. I. Bloom, Z. Zhang, K. M. Hastie, A. Grifoni, D. Weiskopf, S. B. Wells, B. B. Ural, N. Lam, P. A. Szabo, P.

Dogra, Y. S. Lee, J. I. Gray, M. C. Bradley, M. A. Brusko, T. M. Brusko, E. O. Saphire, T. J. Connors, A. Sette, S. Crotty, D. L. Farber, SARS-CoV-2 infection generates tissue-localized immunological memory in humans. *Sci. Immunol.* **6**, eabl9105 (2021). doi:10.1126/sciimmunol.abl9105 Medline

26. J. Grau-Expósito, N. Sánchez-Gaona, N. Massana, M. Suppi, A. Astorga-Gamaza, D. Perea, J. Rosado, A. Falcó, C. Kirkegaard, A. Torrella, B. Planas, J. Navarro, P. Suanzes, D. Álvarez-Sierra, A. Ayora, I. Sansano, J. Esperalba, C. Andrés, A. Antón, S. Ramón Y Cajal, B. Almirante, R. Pujol-Borrell, V. Falcó, J. Burgos, M. J. Buzón, M. Genescà, Peripheral and lung resident memory T cell responses against SARS-CoV-2. *Nat. Commun.* **12**, 3010 (2021). doi:10.1038/s41467-021-23333-3 Medline
27. J. Matschke, M. Lütgehetmann, C. Hagel, J. P. Sperhake, A. S. Schröder, C. Edler, H. Mushumba, A. Fitzek, L. Allweiss, M. Dandri, M. Dottermusch, A. Heinemann, S. Pfefferle, M. Schwabenland, D. Sumner Magruder, S. Bonn, M. Prinz, C. Gerloff, K. Püschel, S. Krasemann, M. Aepfelbacher, M. Glatzel, Neuropathology of patients with COVID-19 in Germany: A post-mortem case series. *Lancet Neurol.* **19**, 919–929 (2020). doi:10.1016/S1474-4422(20)30308-2 Medline
28. S. S. Mukerji, I. H. Solomon, What can we learn from brain autopsies in COVID-19? *Neurosci. Lett.* **742**, 135528 (2021). doi:10.1016/j.neulet.2020.135528 Medline
29. M. Remmelink, R. De Mendonça, N. D'Haene, S. De Clercq, C. Verocq, L. Lebrun, P. Lavis, M. L. Racu, A. L. Trépant, C. Maris, S. Rorive, J. C. Goffard, O. De Witte, L. Peluso, J. L. Vincent, C. Decaestecker, F. S. Taccone, I. Salmon, Unspecific post-mortem findings despite multiorgan viral spread in COVID-19 patients. *Crit. Care* **24**, 495 (2020). doi:10.1186/s13054-020-03218-5 Medline
30. X. H. Yao, T. Luo, Y. Shi, Z. C. He, R. Tang, P. P. Zhang, J. Cai, X. D. Zhou, D. P. Jiang, X. C. Fei, X. Q. Huang, L. Zhao, H. Zhang, H. B. Wu, Y. Ren, Z. H. Liu, H. R. Zhang, C. Chen, W. J. Fu, H. Li, X. Y. Xia, R. Chen, Y. Wang, X. D. Liu, C. L. Yin, Z. X. Yan, J. Wang, R. Jing, T. S. Li, W. Q. Li, C. F. Wang, Y. Q. Ding, Q. Mao, D. Y. Zhang, S. Y. Zhang, Y. F. Ping, X. W. Bian, A cohort autopsy study defines COVID-19 systemic pathogenesis. *Cell Res.* **31**, 836–846 (2021). doi:10.1038/s41422-021-00523-8 Medline
31. S. Stein, S. Ramelli, A. Grazioli, J.-Y. Chung, M. Singh, C. K. Yinda, C. Winkler, J. Dickey, K. Ylaya, S. H. Ko, A. Platt, P. Burbelo, M. Quezado, S. Pittaluga, M. Purcell, V. Munster, F. Belinky, M. Ramos-Benitez, E. Boritz, D. Herr, J. Rabin, K. Saharia, R. Madathil, A. Tabatabai, S. Soherwardi, M. McCurdy, K. Peterson, J. Cohen, E. de Wit, K. Vannella, S. Hewitt, D. Kleiner, D. Chertow, SARS-CoV-2 infection and persistence throughout the human body and brain. *Nature preprint*, (2021).
32. J. Zheng, L. R. Wong, K. Li, A. K. Verma, M. E. Ortiz, C. Wohlford-Lenane, M. R. Leidinger, C. M. Knudson, D. K. Meyerholz, P. B. McCray Jr., S. Perlman, COVID-19 treatments and pathogenesis including anosmia in K18-hACE2 mice. *Nature* **589**, 603–607 (2021). doi:10.1038/s41586-020-2943-z Medline
33. L. Bao, W. Deng, B. Huang, H. Gao, J. Liu, L. Ren, Q. Wei, P. Yu, Y. Xu, F. Qi, Y. Qu, F. Li, Q. Lv, W. Wang, J. Xue, S. Gong, M. Liu, G. Wang, S. Wang, Z. Song, L. Zhao, P. Liu, L. Zhao, F. Ye, H. Wang, W. Zhou, N. Zhu, W. Zhen, H. Yu, X. Zhang, L. Guo, L. Chen, C. Wang, Y. Wang, X. Wang, Y. Xiao, Q. Sun, H. Liu, F. Zhu, C. Ma, L. Yan, M. Yang, J. Han, W. Xu, W. Tan, X. Peng, Q. Jin, G. Wu, C. Qin, The pathogenicity of SARS-CoV-2 in hACE2 transgenic mice. *Nature* **583**, 830–833 (2020). doi:10.1038/s41586-020-2312-y Medline
34. E. S. Winkler, A. L. Bailey, N. M. Kafai, S. Nair, B. T. McCune, J. Yu, J. M. Fox, R. E. Chen, J. T. Earnest, S. P. Keeler, J. H. Ritter, L. I. Kang, S. Dort, A. Robichaud, R. Head, M. J. Holtzman, M. S. Diamond, SARS-CoV-2 infection of human ACE2-transgenic mice causes severe lung inflammation and impaired function. *Nat. Immunol.* **21**, 1327–1335 (2020). doi:10.1038/s41590-020-0778-2 Medline
35. J. Sun, Z. Zhuang, J. Zheng, K. Li, R. L. Wong, D. Liu, J. Huang, J. He, A. Zhu, J. Zhao, X. Li, Y. Xi, R. Chen, A. N. Alshukairi, Z. Chen, Z. Zhang, C. Chen, X. Huang, F. Li, X. Lai, D. Chen, L. Wen, J. Zhuo, Y. Zhang, Y. Wang, S. Huang, J. Dai, Y. Shi, K. Zheng, M. R. Leidinger, J. Chen, Y. Li, N. Zhong, D. K. Meyerholz, P. B. McCray Jr., S. Perlman, J. Zhao, Generation of a Broadly Useful Model for COVID-19 Pathogenesis, Vaccination, and Treatment. *Cell* **182**, 734–743.e5 (2020). doi:10.1016/j.cell.2020.06.010 Medline
36. B. Israelow, E. Song, T. Mao, P. Lu, A. Meir, F. Liu, M. M. Alfajaro, J. Wei, H. Dong, R. J. Homer, A. Ring, C. B. Wilen, A. Iwasaki, Mouse model of SARS-CoV-2 reveals inflammatory role of type I interferon signaling. *J. Exp. Med.* **217**, e20201241 (2020). doi:10.1084/jem.20201241 Medline
37. M. Imai, K. Iwatsuki-Horimoto, M. Hatta, S. Loeber, P. J. Halfmann, N. Nakajima, T. Watanabe, M. Ujie, K. Takahashi, M. Ito, S. Yamada, S. Fan, S. Chiba, M. Kuroda, L. Guan, K. Takada, T. Armbrust, A. Balogh, Y. Furusawa, M. Okuda, H. Ueki, A. Yasuhara, Y. Sakai-Tagawa, T. J. S. Lopes, M. Kiso, S. Yamayoshi, N. Kinoshita, N. Ohmagari, S. I. Hattori, M. Takeda, H. Mitsuya, F. Krammer, T. Suzuki, Y. Kawaoka, Syrian hamsters as a small animal model for SARS-CoV-2 infection and countermeasure development. *Proc. Natl. Acad. Sci. U.S.A.* **117**, 16587–16595 (2020). doi:10.1073/pnas.2009799117 Medline
38. S. F. Sia, L. M. Yan, A. W. H. Chin, K. Fung, K. T. Choy, A. Y. L. Wong, P. Kaewpreedee, R. A. P. M. Perera, L. L. M. Poon, J. M. Nicholls, M. Peiris, H. L. Yen, Pathogenesis and transmission of SARS-CoV-2 in golden hamsters. *Nature* **583**, 834–838 (2020). doi:10.1038/s41586-020-2342-5 Medline
39. J. F. Chan, A. J. Zhang, S. Yuan, V. K. Poon, C. C. Chan, A. C. Lee, W. M. Chan, Z. Fan, H. W. Tsoi, L. Wen, R. Liang, J. Cao, Y. Chen, K. Tang, C. Luo, J. P. Cai, K. H. Kok, H. Chu, K. H. Chan, S. Sridhar, Z. Chen, H. Chen, K. K. To, K. Y. Yuen, Simulation of the Clinical and Pathological Manifestations of Coronavirus Disease 2019 (COVID-19) in a Golden Syrian Hamster Model: Implications for Disease Pathogenesis and Transmissibility. *Clin. Infect. Dis.* **71**, 2428–2446 (2020). doi:10.1093/cid/ciaa644 Medline
40. K. A. Ryan, K. R. Bewley, S. A. Fotheringham, G. S. Slack, P. Brown, Y. Hall, N. I. Wand, A. C. Marriott, B. E. Cavell, J. A. Tree, L. Allen, M. J. Aram, T. J. Bean, E. Brunt, K. R. Buttigieg, D. P. Carter, R. Cobb, N. S. Coombes, S. J. Findlay-Wilson, K. J. Godwin, K. E. Gooch, J. Gouriet, R. Halkerston, D. J. Harris, T. H. Hender, H. E. Humphries, L. Hunter, C. M. K. Ho, C. L. Kennard, S. Leung, S. Longet, D. Ngabo, K. L. Osman, J. Paterson, E. J. Penn, S. T. Pullan, E. Rayner, O. Skinner, K. Steeds, I. Taylor, T. Tipton, S. Thomas, C. Turner, R. J. Watson, N. R. Wiblin, S. Charlton, B. Hallis, J. A. Hiscox, S. Funnell, M. J. Dennis, C. J. Whittaker, M. G. Catton, J. Druce, F. J. Salguero, M. W. Carroll, Dose-dependent response to infection with SARS-CoV-2 in the ferret model and evidence of protective immunity. *Nat. Commun.* **12**, 81 (2021). doi:10.1038/s41467-020-20439-y Medline
41. Y. I. Kim, S. G. Kim, S. M. Kim, E. H. Kim, S. J. Park, K. M. Yu, J. H. Chang, E. J. Kim, S. Lee, M. A. B. Casel, J. Um, M. S. Song, H. W. Jeong, V. D. Lai, Y. Kim, B. S. Chin, J. S. Park, K. H. Chung, S. S. Foo, H. Poo, I. P. Mo, O. J. Lee, R. J. Webby, J. U. Jung, Y. K. Choi, Infection and Rapid Transmission of SARS-CoV-2 in Ferrets. *Cell Host Microbe* **27**, 704–709.e2 (2020). doi:10.1016/j.chom.2020.03.023 Medline
42. V. J. Munster, F. Feldmann, B. N. Williamson, N. van Doremalen, L. Pérez-Pérez, J. Schulz, K. Meade-White, A. Okumura, J. Callison, B. Brumbaugh, V. A. Avanzato, R. Rosenke, P. W. Hanley, G. Saturday, D. Scott, E. R. Fischer, E. de Wit, Respiratory disease in rhesus macaques inoculated with SARS-CoV-2. *Nature* **585**, 268–272 (2020). doi:10.1038/s41586-020-2324-7 Medline
43. P. Yu, F. Qi, Y. Xu, F. Li, P. Liu, J. Liu, L. Bao, W. Deng, H. Gao, Z. Xiang, C. Xiao, Q. Lv, S. Gong, J. Liu, Z. Song, Y. Qu, J. Xue, Q. Wei, M. Liu, G. Wang, S. Wang, H. Yu, X. Liu, B. Huang, W. Wang, L. Zhao, H. Wang, F. Ye, W. Zhou, W. Zhen, J. Han, G. Wu, Q. Jin, J. Wang, W. Tan, C. Qin, Age-related rhesus macaque models of COVID-19. *Animal Model. Exp. Med.* **3**, 93–97 (2020). doi:10.1002/ame2.12108 Medline
44. M. Aid, K. Busman-Sahay, S. J. Vidal, Z. Maliga, S. Bondoc, C. Starke, M. Terry, C. A. Jacobson, L. Wrijil, S. Ducat, O. R. Brook, A. D. Miller, M. Porto, K. L. Pellegrini, M. Pino, T. N. Hoang, A. Chandrashekar, S. Patel, K. Stephenson, S. E. Bosinger, H. Andersen, M. G. Lewis, J. L. Hecht, P. K. Sorger, A. J. Martinot, J. D. Estes, D. H. Barouch, Vascular Disease and Thrombosis in SARS-CoV-2-Infected Rhesus Macaques. *Cell* **183**, 1354–1366.e13 (2020). doi:10.1016/j.cell.2020.10.005 Medline
45. D. K. Singh, B. Singh, S. R. Ganatra, M. Gazi, J. Cole, R. Thippeshappa, K. J. Alfson, E. Clemmons, O. Gonzalez, R. Escobedo, T. H. Lee, A. Chatterjee, Y. Goez-Gazi, R. Sharan, M. Gough, C. Alvarez, A. Blakley, J. Ferdin, C. Bartley, H. Staples, L. Parodi, J. Callery, A. Mannino, B. Klaffke, P. Escareno, R. N. Platt 2nd, V. Hodara, J. Scordo, S. Gautam, A. G. Vilanova, A. Olmo-Fontanez, A. Schami, A. Oyejide, D. K. Ajithdoss, R. Copin, A. Baum, C. Kyratsous, X. Alvarez, M. Ahmed, B. Rosa, A. Goodroe, J. Dutton, S. Hall-Ursone, P. A. Frost, A. K. Voges, C. N. Ross, K. Sayers, C. Chen, C. Hallam, S. A. Khader, M. Mitreva, T. J. C. Anderson, L. Martinez-Sobrido, J. L. Patterson, J. Turner, J. B. Torrelles, E. J. Dick Jr., K. Brasky, L. S. Schlesinger, L. D. Giavedoni, R. Carrion Jr., D. Kaushal, Responses to acute infection with SARS-CoV-2 in the lungs of rhesus macaques, baboons and marmosets. *Nat. Microbiol.* **6**, 73–86 (2021). doi:10.1038/s41564-020-00841-4 Medline
46. R. V. Blair, M. Vaccari, L. A. Doyle-Meyers, C. J. Roy, K. Russell-Lodrigue, M. Fahlberg, C. J. Monjure, B. Beddingfield, K. S. Plante, J. A. Plante, S. C. Weaver, X.

Qin, C. C. Midkiff, G. Lehmicke, N. Golden, B. Threeton, T. Penney, C. Allers, M. B. Barnes, M. Pattison, P. K. Datta, N. J. Maness, A. Birnbaum, T. Fischer, R. P. Bohm, J. Rappaport, Acute Respiratory Distress in Aged, SARS-CoV-2-Infected African Green Monkeys but Not Rhesus Macaques. *Am. J. Pathol.* **191**, 274–282 (2021). doi:10.1016/j.ajpath.2020.10.016 Medline

47. B. Rockx, T. Kuiken, S. Herfst, T. Bestebroer, M. M. Lamers, B. B. Oude Munnink, D. de Meulder, G. van Amerongen, J. van den Brand, N. M. A. Okba, D. Schipper, P. van Run, L. Leijten, R. Sikkema, E. Verschoor, B. Verstrepen, W. Bogers, J. Langermans, C. Drosten, M. Fentener van Vlissingen, R. Fouchier, R. de Swart, M. Koopmans, B. L. Haagmans, Comparative pathogenesis of COVID-19, MERS, and SARS in a nonhuman primate model. *Science* **368**, 1012–1015 (2020). doi:10.1126/science.abb7314 Medline
48. E. Speranza, B. N. Williamson, F. Feldmann, G. L. Sturdevant, L. Pérez-Pérez, K. Meade-White, B. J. Smith, J. Lovaglio, C. Martens, V. J. Munster, A. Okumura, C. Shaia, H. Feldmann, S. M. Best, E. de Wit, Single-cell RNA sequencing reveals SARS-CoV-2 infection dynamics in lungs of African green monkeys. *Sci. Transl. Med.* **13**, eabe8146 (2021). doi:10.1126/scitranslmed.abe8146 Medline
49. A. L. Hartman, S. Nambulli, C. M. McMillen, A. G. White, N. L. Tilston-Lunel, J. R. Albe, E. Cottle, M. D. Dunn, L. J. Frye, T. H. Gilliland, E. L. Olsen, K. J. O'Malley, M. M. Schwarz, J. A. Tomko, R. C. Walker, M. Xia, M. S. Hartman, E. Klein, C. A. Scanga, J. L. Flynn, W. B. Klimstra, A. K. McElroy, D. S. Reed, W. P. Duprex, SARS-CoV-2 infection of African green monkeys results in mild respiratory disease discernible by PET/CT imaging and shedding of infectious virus from both respiratory and gastrointestinal tracts. *PLOS Pathog.* **16**, e1008903 (2020). doi:10.1371/journal.ppat.1008903 Medline
50. R. W. Cross, K. N. Agans, A. N. Prasad, V. Borisevich, C. Woolsey, D. J. Deer, N. S. Dobias, J. B. Geisbert, K. A. Fenton, T. W. Geisbert, Intranasal exposure of African green monkeys to SARS-CoV-2 results in acute phase pneumonia with shedding and lung injury still present in the early convalescence phase. *Virol. J.* **17**, 125 (2020). doi:10.1186/s12985-020-01396-w Medline
51. M. D. Fahlberg, R. V. Blair, L. A. Doyle-Meyers, C. C. Midkiff, G. Zenere, K. E. Russell-Lodrigue, C. J. Monjure, E. H. Haupt, T. P. Penney, G. Lehmicke, B. M. Threeton, N. Golden, P. K. Datta, C. J. Roy, R. P. Bohm, N. J. Maness, T. Fischer, J. Rappaport, M. Vaccari, Cellular events of acute, resolving or progressive COVID-19 in SARS-CoV-2 infected non-human primates. *Nat. Commun.* **11**, 6078 (2020). doi:10.1038/s41467-020-19967-4 Medline
52. M. A. Stammes, J. H. Lee, L. Meijer, J. L. Flynn, C. Mani, I. Crozier, J. H. Kuhn, T. Naninck, L. A. Doyle-Meyers, A. G. White, H. J. Borish, A. L. Hartman, X. Alvarez, S. Ganatra, D. Kaushal, R. P. Bohm, R. le Grand, C. A. Scanga, J. A. M. Langermans, R. E. Bontrop, C. L. Finch, Medical imaging of pulmonary disease in SARS-CoV-2-exposed nonhuman primates. *Trends Mol. Med.* (2021). Medline
53. K. S. Corbett, B. Flynn, K. E. Foulds, J. R. Francica, S. Boyoglu-Barnum, A. P. Werner, B. Flach, S. O'Connell, K. W. Bock, M. Minai, B. M. Nagata, H. Andersen, D. R. Martinez, A. T. Noe, N. Douek, M. M. Donaldson, N. N. Nji, G. S. Alvarado, D. K. Edwards, D. R. Flebbe, E. Lamb, N. A. Doria-Rose, B. C. Lin, M. K. Louder, S. O'Dell, S. D. Schmidt, E. Phung, L. A. Chang, C. Yap, J. M. Todd, L. Pessaint, A. Van Ry, S. Browne, J. Greenhouse, T. Putman-Taylor, A. Strasbaugh, T. A. Campbell, A. Cook, A. Dodson, K. Steingrebe, W. Shi, Y. Zhang, O. M. Abiona, L. Wang, A. Pegu, E. S. Yang, K. Leung, T. Zhou, I. T. Teng, A. Widge, I. Gordon, L. Novik, R. A. Gillespie, R. J. Loomis, J. I. Moliva, G. Stewart-Jones, S. Himansu, W. P. Kong, M. C. Nason, K. M. Morabito, T. J. Ruckwardt, J. E. Ledgerwood, M. R. Gaudinski, P. D. Kwong, J. R. Mascola, A. Carfi, M. G. Lewis, R. S. Baric, A. McDermott, I. N. Moore, N. J. Sullivan, M. Roederer, R. A. Seder, B. S. Graham, Evaluation of the mRNA-1273 Vaccine against SARS-CoV-2 in Nonhuman Primates. *N. Engl. J. Med.* **383**, 1544–1555 (2020). doi:10.1056/NEJMoa2024671 Medline
54. K. S. Corbett, M. C. Nason, B. Flach, M. Gagne, S. O'Connell, T. S. Johnston, S. N. Shah, V. V. Edara, K. Floyd, L. Lai, C. McDanal, J. R. Francica, B. Flynn, K. Wu, A. Choi, M. Koch, O. M. Abiona, A. P. Werner, J. I. Moliva, S. F. Andrew, M. M. Donaldson, J. Fintzi, D. R. Flebbe, E. Lamb, A. T. Noe, S. T. Nurmukhambetova, S. J. Provost, A. Cook, A. Dodson, A. Faudree, J. Greenhouse, S. Kar, L. Pessaint, M. Porto, K. Steingrebe, D. Valentin, S. Zouantcha, K. W. Bock, M. Minai, B. M. Nagata, R. van de Wetering, S. Boyoglu-Barnum, K. Leung, W. Shi, E. S. Yang, Y. Zhang, J. M. Todd, L. Wang, G. S. Alvarado, H. Andersen, K. E. Foulds, D. K. Edwards, J. R. Mascola, I. N. Moore, M. G. Lewis, A. Carfi, D. Montefiori, M. S. Suthar, A. McDermott, M. Roederer, N. J. Sullivan, D. C. Douek, B. S. Graham, R. A. Seder, Immune correlates of protection by mRNA-1273 vaccine against SARS-CoV-2 in nonhuman primates. *Science* **373**, eabj0299 (2021). doi:10.1126/science.abj0299 Medline
55. K. S. Corbett, A. P. Werner, S. O. Connell, M. Gagne, L. Lai, J. I. Moliva, B. Flynn, A. Choi, M. Koch, K. E. Foulds, S. F. Andrew, D. R. Flebbe, E. Lamb, S. T. Nurmukhambetova, S. J. Provost, K. W. Bock, M. Minai, B. M. Nagata, A. V. Ry, Z. Flinchbaugh, T. S. Johnston, E. B. Mokhtari, P. Mudvari, A. R. Henry, F. Laboune, B. Chang, M. Porto, J. Wear, G. S. Alvarado, S. Boyoglu-Barnum, J. M. Todd, B. Bart, A. Cook, A. Dodson, L. Pessaint, K. Steingrebe, S. Elbashir, M. Sriparna, A. Pekosz, H. Andersen, K. Wu, D. K. Edwards, S. Kar, M. G. Lewis, E. Boritz, I. N. Moore, A. Carfi, M. S. Suthar, A. McDermott, M. Roederer, M. C. Nason, N. J. Sullivan, D. C. Douek, B. S. Graham, R. A. Seder, mRNA-1273 protects against SARS-CoV-2 beta infection in nonhuman primates. *Nat. Immunol.* **22**, 1306–1315 (2021). doi:10.1038/s41590-021-01021-0 Medline
56. M. Gagne, K. S. Corbett, B. J. Flynn, K. E. Foulds, D. A. Wagner, S. F. Andrew, J. M. Todd, C. C. Honeycutt, L. McCormick, S. T. Nurmukhambetova, M. E. Davis-Gardner, L. Pessaint, K. W. Bock, B. M. Nagata, M. Minai, A. P. Werner, J. I. Moliva, C. Tucker, C. G. Lorang, B. Zhao, E. McCarthy, A. Cook, A. Dodson, I. T. Teng, P. Mudvari, J. Roberts-Torres, F. Laboune, L. Wang, A. Goode, S. Kar, S. Boyoglu-Barnum, E. S. Yang, W. Shi, A. Ploquin, N. Doria-Rose, A. Carfi, J. R. Mascola, E. A. Boritz, D. K. Edwards, H. Andersen, M. G. Lewis, M. S. Suthar, B. S. Graham, M. Roederer, I. N. Moore, M. C. Nason, N. J. Sullivan, D. C. Douek, R. A. Seder, Protection from SARS-CoV-2 Delta one year after mRNA-1273 vaccination in rhesus macaques coincides with anamnestic antibody response in the lung. *Cell* **185**, 113–130.e15 (2022). doi:10.1016/j.cell.2021.12.002 Medline
57. J. Yu, L. H. Tostanoski, L. Peter, N. B. Mercado, K. McMahan, S. H. Mahrokhian, J. P. Nkolola, J. Liu, Z. Li, A. Chandrashekar, D. R. Martinez, C. Loos, C. Atyeo, S. Fischinger, J. S. Burke, M. D. Slein, Y. Chen, A. Zuiani, F. J. N. Lelis, M. Travers, S. Habibi, L. Pessaint, A. Van Ry, K. Blade, R. Brown, A. Cook, B. Finneyfrock, A. Dodson, E. Teow, J. Velasco, R. Zahn, F. Wegmann, E. A. Bondzie, G. Dagotto, M. S. Gebre, X. He, C. Jacob-Dolan, M. Kirilova, N. Kordana, Z. Lin, L. F. Maxfield, F. Nampanya, R. Nityanandam, J. D. Ventura, H. Wan, Y. Cai, B. Chen, A. G. Schmidt, D. R. Wesemann, R. S. Baric, G. Alter, H. Andersen, M. G. Lewis, D. H. Barouch, DNA vaccine protection against SARS-CoV-2 in rhesus macaques. *Science* **369**, 806–811 (2020). doi:10.1126/science.abc6284 Medline
58. N. B. Mercado, R. Zahn, F. Wegmann, C. Loos, A. Chandrashekar, J. Yu, J. Liu, L. Peter, K. McMahan, L. H. Tostanoski, X. He, D. R. Martinez, L. Rutten, R. Bos, D. van Manen, J. Vellinga, J. Custers, J. P. Langedijk, T. Kwaks, M. J. G. Bakkers, D. Zuijdgeest, S. K. Rosendahl Huber, C. Atyeo, S. Fischinger, J. S. Burke, J. Feldman, B. M. Hauser, T. M. Caradonna, E. A. Bondzie, G. Dagotto, M. S. Gebre, E. Hoffman, C. Jacob-Dolan, M. Kirilova, Z. Li, Z. Lin, S. H. Mahrokhian, L. F. Maxfield, F. Nampanya, R. Nityanandam, J. P. Nkolola, S. Patel, J. D. Ventura, K. Verrington, H. Wan, L. Pessaint, A. Van Ry, K. Blade, A. Strasbaugh, M. Cabus, R. Brown, A. Cook, S. Zouantchangadou, E. Teow, H. Andersen, M. G. Lewis, Y. Cai, B. Chen, A. G. Schmidt, R. K. Reeves, R. S. Baric, D. A. Lauffenburger, G. Alter, P. Stoffels, M. Mammen, J. Van Hoof, H. Schuitemaker, D. H. Barouch, Single-shot Ad26 vaccine protects against SARS-CoV-2 in rhesus macaques. *Nature* **586**, 583–588 (2020). doi:10.1038/s41586-020-2607-z Medline
59. K. McMahan, J. Yu, N. B. Mercado, C. Loos, L. H. Tostanoski, A. Chandrashekar, J. Liu, L. Peter, C. Atyeo, A. Zhu, E. A. Bondzie, G. Dagotto, M. S. Gebre, C. Jacob-Dolan, Z. Li, F. Nampanya, S. Patel, L. Pessaint, A. Van Ry, K. Blade, J. Yalley-Ogunro, M. Cabus, R. Brown, A. Cook, E. Teow, H. Andersen, M. G. Lewis, D. A. Lauffenburger, G. Alter, D. H. Barouch, Correlates of protection against SARS-CoV-2 in rhesus macaques. *Nature* **590**, 630–634 (2021). doi:10.1038/s41586-020-03041-6 Medline
60. N. van Doremalen, T. Lambe, A. Spencer, S. Belij-Rammerstorfer, J. N. Purushotham, J. R. Port, V. A. Avanzato, T. Bushmaker, A. Flaxman, M. Ulaszewska, F. Feldmann, E. R. Allen, H. Sharpe, J. Schulz, M. Holbrook, A. Okumura, K. Meade-White, L. Pérez-Pérez, N. J. Edwards, D. Wright, C. Bissett, C. Gilbride, B. N. Williamson, R. Rosenke, D. Long, A. Ishwarbhai, R. Kailath, L. Rose, S. Morris, C. Powers, J. Lovaglio, P. W. Hanley, D. Scott, G. Saturday, E. de Wit, S. C. Gilbert, V. J. Munster, ChAdOx1 nCoV-19 vaccine prevents SARS-CoV-2 pneumonia in rhesus macaques. *Nature* **586**, 578–582 (2020). doi:10.1038/s41586-020-2608-y Medline
61. W. Deng, L. Bao, J. Liu, C. Xiao, J. Liu, J. Xue, Q. Lv, F. Qi, H. Gao, P. Yu, Y. Xu, Y. Qu,

F. Li, Z. Xiang, H. Yu, S. Gong, M. Liu, G. Wang, S. Wang, Z. Song, Y. Liu, W. Zhao, Y. Han, L. Zhao, X. Liu, Q. Wei, C. Qin, Primary exposure to SARS-CoV-2 protects against reinfection in rhesus macaques. *Science* **369**, 818–823 (2020). doi:10.1126/science.abc5343 Medline

62. A. Chandrashekar, J. Liu, J. Yu, K. McMahan, L. H. Tostanoski, C. Jacob-Dolan, N. B. Mercado, T. Anioke, A. Chang, S. Gardner, V. M. Giffin, D. L. Hope, F. Nampanya, S. Patel, O. Sanborn, D. Sellers, H. Wan, A. J. Martinot, J. J. Baczenas, S. L. O'Connor, L. Pessaint, D. Valentin, B. Espina, L. Wattay, M. G. Ferrari, R. Brown, A. Cook, D. Bueno-Wilkerson, E. Teow, H. Andersen, M. G. Lewis, D. H. Barouch, Prior infection with SARS-CoV-2 WA1/2020 partially protects rhesus macaques against reinfection with B.1.1.7 and B.1.351 variants. *Sci. Transl. Med.* **13**, eabj2641 (2021). doi:10.1126/scitranslmed.abj2641 Medline
63. A. Chandrashekar, J. Liu, A. J. Martinot, K. McMahan, N. B. Mercado, L. Peter, L. H. Tostanoski, J. Yu, Z. Maliga, M. Nekorchuk, K. Busman-Sahay, M. Terry, L. M. Wrijil, S. Ducat, D. R. Martinez, C. Atyeo, S. Fischinger, J. S. Burke, M. D. Slein, L. Pessaint, A. Van Ry, J. Greenhouse, T. Taylor, K. Blade, A. Cook, B. Finneyfrock, R. Brown, E. Teow, J. Velasco, R. Zahn, F. Wegmann, P. Abbink, E. A. Bondzie, G. Dagotto, M. S. Gebre, X. He, C. Jacob-Dolan, N. Kordana, Z. Li, M. A. Lifton, S. H. Mahrokhian, L. F. Maxfield, R. Nityanandam, J. P. Nkolola, A. G. Schmidt, A. D. Miller, R. S. Baric, G. Alter, P. K. Sorger, J. D. Estes, H. Andersen, M. G. Lewis, D. H. Barouch, SARS-CoV-2 infection protects against rechallenge in rhesus macaques. *Science* **369**, 812–817 (2020). doi:10.1126/science.abc4776 Medline
64. K. J. Hasenkrug, F. Feldmann, L. Myers, M. L. Santiago, K. Guo, B. S. Barrett, K. L. Mickens, A. Carmody, A. Okumura, D. Rao, M. M. Collins, R. J. Messer, J. Lovaglio, C. Shaia, R. Rosenke, N. van Doremalen, C. Clancy, G. Saturday, P. Hanley, B. J. Smith, K. Meade-White, W. L. Shupert, D. W. Hawman, H. Feldmann, Recovery from Acute SARS-CoV-2 Infection and Development of Anamnestic Immune Responses in T Cell-Depleted Rhesus Macaques. *mBio* **12**, e0150321 (2021). doi:10.1128/mBio.01503-21 Medline
65. E. Kvedaraite, L. Hertwig, I. Sinha, A. Ponzetta, I. Hed Myrberg, M. Lourda, M. Dzidic, M. Akber, J. Klingström, E. Folkesson, J. R. Muvva, P. Chen, S. Gredmark-Russ, S. Brighenti, A. Norrby-Teglund, L. I. Eriksson, O. Rooyackers, S. Aleman, K. Strålin, H. G. Ljunggren, F. Ginhoux, N. K. Björkström, J. I. Henter, M. Svensson; Karolinska KI/K COVID-19 Study Group, Major alterations in the mononuclear phagocyte landscape associated with COVID-19 severity. *Proc. Natl. Acad. Sci. U.S.A.* **118**, e2018587118 (2021). doi:10.1073/pnas.2018587118 Medline
66. G. Xu, F. Qi, H. Li, Q. Yang, H. Wang, X. Wang, X. Liu, J. Zhao, X. Liao, Y. Liu, L. Liu, S. Zhang, Z. Zhang, The differential immune responses to COVID-19 in peripheral and lung revealed by single-cell RNA sequencing. *Cell Discov.* **6**, 73 (2020). doi:10.1038/s41421-020-00225-2 Medline
67. M. Collin, V. Bigley, Human dendritic cell subsets: An update. *Immunology* **154**, 3–20 (2018). doi:10.1111/imm.12888 Medline
68. A. Grifoni, J. Sidney, Y. Zhang, R. H. Scheuermann, B. Peters, A. Sette, A Sequence Homology and Bioinformatic Approach Can Predict Candidate Targets for Immune Responses to SARS-CoV-2. *Cell Host Microbe* **27**, 671–680.e2 (2020). doi:10.1016/j.chom.2020.03.002 Medline
69. A. Grifoni, D. Weiskopf, S. I. Ramirez, J. Mateus, J. M. Dan, C. R. Moderbacher, S. A. Rawlings, A. Sutherland, L. Premkumar, R. S. Jadi, D. Marrama, A. M. de Silva, A. Frazier, A. F. Carlin, J. A. Greenbaum, B. Peters, F. Krammer, D. M. Smith, S. Crotty, A. Sette, Targets of T Cell Responses to SARS-CoV-2 Coronavirus in Humans with COVID-19 Disease and Unexposed Individuals. *Cell* **181**, 1489–1501.e15 (2020). doi:10.1016/j.cell.2020.05.015 Medline
70. L. K. Beura, N. J. Fares-Frederickson, E. M. Steinert, M. C. Scott, E. A. Thompson, K. A. Fraser, J. M. Schenkel, V. Vezys, D. Masopust, $CD4^+$ resident memory T cells dominate immunosurveillance and orchestrate local recall responses. *J. Exp. Med.* **216**, 1214–1229 (2019). doi:10.1084/jem.20181365 Medline
71. B. V. Kumar, W. Ma, M. Miron, T. Granot, R. S. Guyer, D. J. Carpenter, T. Senda, X. Sun, S. H. Ho, H. Lerner, A. L. Friedman, Y. Shen, D. L. Farber, Human Tissue-Resident Memory T Cells Are Defined by Core Transcriptional and Functional Signatures in Lymphoid and Mucosal Sites. *Cell Rep.* **20**, 2921–2934 (2017). doi:10.1016/j.celrep.2017.08.078 Medline
72. K. G. Anderson, H. Sung, C. N. Skon, L. Lefrancois, A. Deisinger, V. Vezys, D. Masopust, Cutting edge: Intravascular staining redefines lung CD8 T cell responses. *J. Immunol.* **189**, 2702–2706 (2012). doi:10.4049/jimmunol.1201682 Medline
73. K. D. Kauffman, M. A. Sallin, S. Sakai, O. Kamenyeva, J. Kabat, D. Weiner, M. Sutphin, D. Schimel, L. Via, C. E. Barry 3rd, T. Wilder-Kofie, I. Moore, R. Moore, D. L. Barber, Defective positioning in granulomas but not lung-homing limits CD4 T-cell interactions with Mycobacterium tuberculosis-infected macrophages in rhesus macaques. *Mucosal Immunol.* **11**, 462–473 (2018). doi:10.1038/mi.2017.60 Medline
74. E. L. Potter, H. P. Gideon, V. Tkachev, G. Fabozzi, A. Chassiakos, C. Petrovas, P. A. Darrah, P. L. Lin, K. E. Foulds, L. S. Kean, J. L. Flynn, M. Roederer, Measurement of leukocyte trafficking kinetics in macaques by serial intravascular staining. *Sci. Transl. Med.* **13**, eabb4582 (2021). doi:10.1126/scitranslmed.abb4582 Medline
75. P. Bost, A. Giladi, Y. Liu, Y. Bendjelal, G. Xu, E. David, R. Blecher-Gonen, M. Cohen, C. Medaglia, H. Li, A. Deczkowska, S. Zhang, B. Schwikowski, Z. Zhang, I. Amit, Host-Viral Infection Maps Reveal Signatures of Severe COVID-19 Patients. *Cell* **181**, 1475–1488.e12 (2020). doi:10.1016/j.cell.2020.05.006 Medline
76. C. Bosteels, K. Neyt, M. Vanheerswynghels, M. J. van Helden, D. Sichien, N. Debeuf, S. De Prijck, V. Bosteels, N. Vandamme, L. Martens, Y. Saeys, E. Louagie, M. Lesage, D. L. Williams, S. C. Tang, J. U. Mayer, F. Ronchese, C. L. Scott, H. Hammad, M. Guilliams, B. N. Lambrecht, Inflammatory Type 2 cDCs Acquire Features of cDC1s and Macrophages to Orchestrate Immunity to Respiratory Virus Infection. *Immunity* **52**, 1039–1056.e9 (2020). doi:10.1016/j.immuni.2020.04.005 Medline
77. J. M. Dan, J. Mateus, Y. Kato, K. M. Hastie, E. D. Yu, C. E. Faliti, A. Grifoni, S. I. Ramirez, S. Haupt, A. Frazier, C. Nakao, V. Rayaprolu, S. A. Rawlings, B. Peters, F. Krammer, V. Simon, E. O. Saphire, D. M. Smith, D. Weiskopf, A. Sette, S. Crotty, Immunological memory to SARS-CoV-2 assessed for up to 8 months after infection. *Science* **371**, eabf4063 (2021). doi:10.1126/science.abf4063 Medline
78. C. H. Hansen, D. Michlmayr, S. M. Gubbels, K. Mølbak, S. Ethelberg, Assessment of protection against reinfection with SARS-CoV-2 among 4 million PCR-tested individuals in Denmark in 2020: A population-level observational study. *Lancet* **397**, 1204–1212 (2021). doi:10.1016/S0140-6736(21)00575-4 Medline
79. J. Vitale, N. Mumoli, P. Clerici, M. De Paschale, I. Evangelista, M. Cei, A. Mazzone, Assessment of SARS-CoV-2 Reinfection 1 Year After Primary Infection in a Population in Lombardy, Italy. *JAMA Intern. Med.* **181**, 1407–1408 (2021). doi:10.1001/jamainternmed.2021.2959 Medline
80. M. M. Sheehan, A. J. Reddy, M. B. Rothberg, Reinfection Rates Among Patients Who Previously Tested Positive for Coronavirus Disease 2019: A Retrospective Cohort Study. *Clin. Infect. Dis.* **73**, 1882–1886 (2021). doi:10.1093/cid/ciab234 Medline
81. T. Nomura, H. Yamamoto, M. Nishizawa, T. T. T. Hau, S. Harada, H. Ishii, S. Seki, M. Nakamura-Hoshi, M. Okazaki, S. Daigen, A. Kawana-Tachikawa, N. Nagata, N. Iwata-Yoshikawa, N. Shiwa, S. Iida, H. Katano, T. Suzuki, E. S. Park, K. Maeda, Y. Suzaki, Y. Ami, T. Matano, Subacute SARS-CoV-2 replication can be controlled in the absence of CD8+ T cells in cynomolgus macaques. *PLOS Pathog.* **17**, e1009668 (2021). doi:10.1371/journal.ppat.1009668 Medline
82. B. Israelow, T. Mao, J. Klein, E. Song, B. Menasche, S. B. Omer, A. Iwasaki, Adaptive immune determinants of viral clearance and protection in mouse models of SARS-CoV-2. *Sci. Immunol.* **6**, eabl4509 (2021). doi:10.1126/sciimmunol.abl4509 Medline
83. R. L. Brocato, L. M. Principe, R. K. Kim, X. Zeng, J. A. Williams, Y. Liu, R. Li, J. M. Smith, J. W. Golden, D. Gangemi, S. Youssef, Z. Wang, J. Glanville, J. W. Hooper, Disruption of Adaptive Immunity Enhances Disease in SARS-CoV-2-Infected Syrian Hamsters. *J. Virol.* **94**, e01683-20 (2020). doi:10.1128/JVI.01683-20 Medline
84. S. Horiuchi, K. Oishi, L. Carrau, J. Frere, R. Møller, M. Panis, B. R. tenOever, Immune memory from SARS-CoV-2 infection in hamsters provides variant-independent protection but still allows virus transmission. *Sci. Immunol.* **6**, eabm3131 (2021). doi:10.1126/sciimmunol.abm3131 Medline
85. J. S. Heitmann, T. Bilich, C. Tandler, A. Nelde, Y. Maringer, M. Marconato, J. Reusch, S. Jager, M. Denk, M. Richter, L. Anton, L. M. Weber, M. Roerden, J. Bauer, J. Rieth, M. Wacker, S. Horber, A. Peter, C. Meisner, I. Fischer, M. W. Loffler, J. Karbach, E. Jager, R. Klein, H. G. Rammensee, H. R. Salih, J. S. Walz, A COVID-19 peptide vaccine for the induction of SARS-CoV-2 T cell immunity. *Nature* (2021). Medline
86. J. Y. Noh, H. W. Jeong, J. H. Kim, E. C. Shin, T cell-oriented strategies for controlling the COVID-19 pandemic. *Nat. Rev. Immunol.* **21**, 687–688 (2021).

doi:10.1038/s41577-021-00625-9 Medline
87. A. Tarke, J. Sidney, N. Methot, E. D. Yu, Y. Zhang, J. M. Dan, B. Goodwin, P. Rubiro, A. Sutherland, E. Wang, A. Frazier, S. I. Ramirez, S. A. Rawlings, D. M. Smith, R. da Silva Antunes, B. Peters, R. H. Scheuermann, D. Weiskopf, S. Crotty, A. Grifoni, A. Sette, Impact of SARS-CoV-2 variants on the total $CD4^+$ and $CD8^+$ T cell reactivity in infected or vaccinated individuals. *Cell Rep. Med.* **2**, 100355 (2021). doi:10.1016/j.xcrm.2021.100355 Medline
88. A. Tarke, C. H. Coelho, Z. Zhang, J. M. Dan, E. D. Yu, N. Methot, N. I. Bloom, B. Goodwin, E. Phillips, S. Mallal, J. Sidney, G. Filaci, D. Weiskopf, R. da Silva Antunes, S. Crotty, A. Grifoni, A. Sette, SARS-CoV-2 vaccination induces immunological T cell memory able to cross-recognize variants from Alpha to Omicron. *Cell* **185**, 847–859.e11 (2022). doi:10.1016/j.cell.2022.01.015 Medline
89. R. Keeton, M. B. Tincho, A. Ngomti, R. Baguma, N. Benede, A. Suzuki, K. Khan, S. Cele, M. Bernstein, F. Karim, S. V. Madzorera, T. Moyo-Gwete, M. Mennen, S. Skelem, M. Adriaanse, D. Mutithu, O. Aremu, C. Stek, E. du Bruyn, M. A. Van Der Mescht, Z. de Beer, T. R. de Villiers, A. Bodenstein, G. van den Berg, A. Mendes, A. Strydom, M. Venter, J. Giandhari, Y. Naidoo, S. Pillay, H. Tegally, A. Grifoni, D. Weiskopf, A. Sette, R. J. Wilkinson, T. de Oliveira, L. G. Bekker, G. Gray, V. Ueckermann, T. Rossouw, M. T. Boswell, J. Bihman, P. L. Moore, A. Sigal, N. A. B. Ntusi, W. A. Burgers, C. Riou, T cell responses to SARS-CoV-2 spike cross-recognize Omicron. *Nature* (2022). doi:10.1038/s41586-022-04460-3 Medline
90. Y. Gao, C. Cai, A. Grifoni, T. R. Müller, J. Niessl, A. Olofsson, M. Humbert, L. Hansson, A. Österborg, P. Bergman, P. Chen, A. Olsson, J. K. Sandberg, D. Weiskopf, D. A. Price, H. G. Ljunggren, A. C. Karlsson, A. Sette, S. Aleman, M. Buggert, Ancestral SARS-CoV-2-specific T cells cross-recognize the Omicron variant. *Nat. Med.* (2022). doi:10.1038/s41591-022-01700-x Medline
91. C. H. GeurtsvanKessel, D. Geers, K. S. Schmitz, A. Z. Mykytyn, M. M. Lamers, S. Bogers, S. Scherbeijn, L. Gommers, R. S. G. Sablerolles, N. N. Nieuwkoop, L. C. Rijsbergen, L. L. A. van Dijk, J. de Wilde, K. Alblas, T. I. Breugem, B. J. A. Rijnders, H. de Jager, D. Weiskopf, P. H. M. van der Kuy, A. Sette, M. P. G. Koopmans, A. Grifoni, B. L. Haagmans, R. D. de Vries, Divergent SARS CoV-2 Omicron-reactive T- and B cell responses in COVID-19 vaccine recipients. *Sci. Immunol.* •••, eabo2202 (2022). doi:10.1126/sciimmunol.abo2202 Medline
92. J. Liu, A. Chandrashekar, D. Sellers, J. Barrett, C. Jacob-Dolan, M. Lifton, K. McMahan, M. Sciacca, H. VanWyk, C. Wu, J. Yu, A. Y. Collier, D. H. Barouch, Vaccines Elicit Highly Conserved Cellular Immunity to SARS-CoV-2 Omicron. *Nature* (2022). doi:10.1038/s41586-022-04465-y Medline
93. K. D. Kauffman, S. Sakai, N. E. Lora, S. Namasivayam, P. J. Baker, O. Kamenyeva, T. W. Foreman, C. E. Nelson, D. Oliveira-de-Souza, C. L. Vinhaes, Z. Yaniv, C. S. Lindestam Arleham, A. Sette, G. J. Freeman, R. Moore, A. Sher, K. D. Mayer-Barber, B. B. Andrade, J. Kabat, L. E. Via, D. L. Barber; NIAID/DIR Tuberculosis Imaging Program, PD-1 blockade exacerbates *Mycobacterium tuberculosis* infection in rhesus macaques. *Sci. Immunol.* **6**, eabf3861 (2021). doi:10.1126/sciimmunol.abf3861 Medline
94. T. Beites, K. O'Brien, D. Tiwari, C. A. Engelhart, S. Walters, J. Andrews, H. J. Yang, M. L. Sutphen, D. M. Weiner, E. K. Dayao, M. Zimmerman, B. Prideaux, P. V. Desai, T. Masquelin, L. E. Via, V. Dartois, H. I. Boshoff, C. E. Barry 3rd, S. Ehrt, D. Schnappinger, Plasticity of the Mycobacterium tuberculosis respiratory chain and its impact on tuberculosis drug development. *Nat. Commun.* **10**, 4970 (2019). doi:10.1038/s41467-019-12956-2 Medline
95. S. Sakai, N. E. Lora, K. D. Kauffman, D. E. Dorosky, S. Oh, S. Namasivayam, F. Gomez, J. D. Fleegle, C. S. L. Arlehamn, A. Sette, A. Sher, G. J. Freeman, L. E. Via, C. E. Barry Iii, D. L. Barber; Tuberculosis Imaging Program, Functional inactivation of pulmonary MAIT cells following 5-OP-RU treatment of non-human primates. *Mucosal Immunol.* **14**, 1055–1066 (2021). doi:10.1038/s41385-021-00425-3 Medline
96. L. E. Via, K. England, D. M. Weiner, D. Schimel, M. D. Zimmerman, E. Dayao, R. Y. Chen, L. E. Dodd, M. Richardson, K. K. Robbins, Y. Cai, D. Hammoud, P. Herscovitch, V. Dartois, J. L. Flynn, C. E. Barry 3rd, A sterilizing tuberculosis treatment regimen is associated with faster clearance of bacteria in cavitary lesions in marmosets. *Antimicrob. Agents Chemother.* **59**, 4181–4189 (2015). doi:10.1128/AAC.00115-15 Medline
97. X. Liu, C. Luongo, Y. Matsuoka, H. S. Park, C. Santos, L. Yang, I. N. Moore, S. Afroz, R. F. Johnson, B. A. P. Lafont, C. Martens, S. M. Best, V. J. Munster, J. Hollý, J. W. Yewdell, C. Le Nouën, S. Munir, U. J. Buchholz, A single intranasal dose of a live-attenuated parainfluenza virus-vectored SARS-CoV-2 vaccine is protective in hamsters. *Proc. Natl. Acad. Sci. U.S.A.* **118**, e2109744118 (2021). doi:10.1073/pnas.2109744118 Medline
98. M. Stoeckius, S. Zheng, B. Houck-Loomis, S. Hao, B. Z. Yeung, W. M. Mauck 3rd, P. Smibert, R. Satija, Cell Hashing with barcoded antibodies enables multiplexing and doublet detection for single cell genomics. *Genome Biol.* **19**, 224 (2018). doi:10.1186/s13059-018-1603-1 Medline

Acknowledgments: Members of the NIAID/DIR Tuberculosis Imaging Program include Ayan Abdi, Emmuanual K. Dayao, Joel D. Fleegle, Felipe Gomez, Michaela K. Piazza, Katelyn M. Repoli, Becky Y. Sloan, Ashley L. Butler, April M. Walker, Danielle M. Weiner, Michael J. Woodcock, and Alexandra Vatthauer. We would like to acknowledge the Center for Cancer Research Sequencing Facility at the Frederick National Laboratory for Cancer Research for performing the sequencing and Drs. Paul Schaughency and Justin Lack of the NIAID Collaborative Bioinformatics Resource for assistance with the bioinformatics. We would like to thank Dr. Rashida Moore for clinical care of the macaques and Drs. Kerry Hilligan and Paul Baker for assistance with S.O.P.s and inactivation method development for SARS-CoV-2 BSL-3 work. **FUNDING:** Funding for this study was provided in part by the Division of Intramural Research/NIAID/NIH project number 1ZIAAI001294-02. A.S. and D.W. were supported by NIH grant contract number 75N9301900065. The content of this publication does not necessarily reflect the views or policies of DHHS, nor does the mention of trade names, commercial products, or organizations imply endorsement by the U.S. Government. **AUTHOR CONTRIBUTIONS:** C.E.N. led the study. C.E.N., J.M.B., L.E.V., and D.L.B. designed the study. C.E.N., S.N., T.W.F., K.D.K., S.S., D.D., and N.E.L. performed experiments. C.E.N., T.W.F., and D.L.B. analyzed data. S.N., A.S., C.E.N., and D.L.B. performed single cell RNA sequencing analysis. N.L.G., B.A.P.L. and R.F.J. performed the PRNT assays. The Tuberculosis Imaging Program (TBIP) managed logistics and performed NHP manipulations including infection, necropsy, PET/CT scanning, and imaging analysis. F.G. and J.D.F. analyzed the PET/CT data. L.E.V. supervised T.B.I.P. and designed the analysis for PET/CT data. C.E.N., S.N., T.W.F, and D.L.B. made figures. E.L.P., M.R., D.W., E.dW., and H.D.H. provided necessary reagents for the completion of the study. C.E.N., S.N. and D.L.B. wrote the manuscript. All authors contributed to editing the manuscript. D.L.B. supervised the study. **COMPETING INTERESTS:** A.S. is a consultant for Gritstone, Flow Pharma, Arcturus, Immunoscape, CellCarta, OxfordImmunotech and Avalia. LJI has filed for patent protection for various aspects of T cell epitope and vaccine design work. All other authors declare no conflict of interest. **DATA AND MATERIALS AVAILABILITY:** Single-cell RNAseq read data are submitted at NCBI GEO under accession GSE196980. All other data needed to support the conclusion of the paper are present in the paper or the Supplementary Materials.

Submitted 10 January 2022
Accepted 4 March 2022
Published First Release 10 March 2022
10.1126/sciimmunol.abo0535

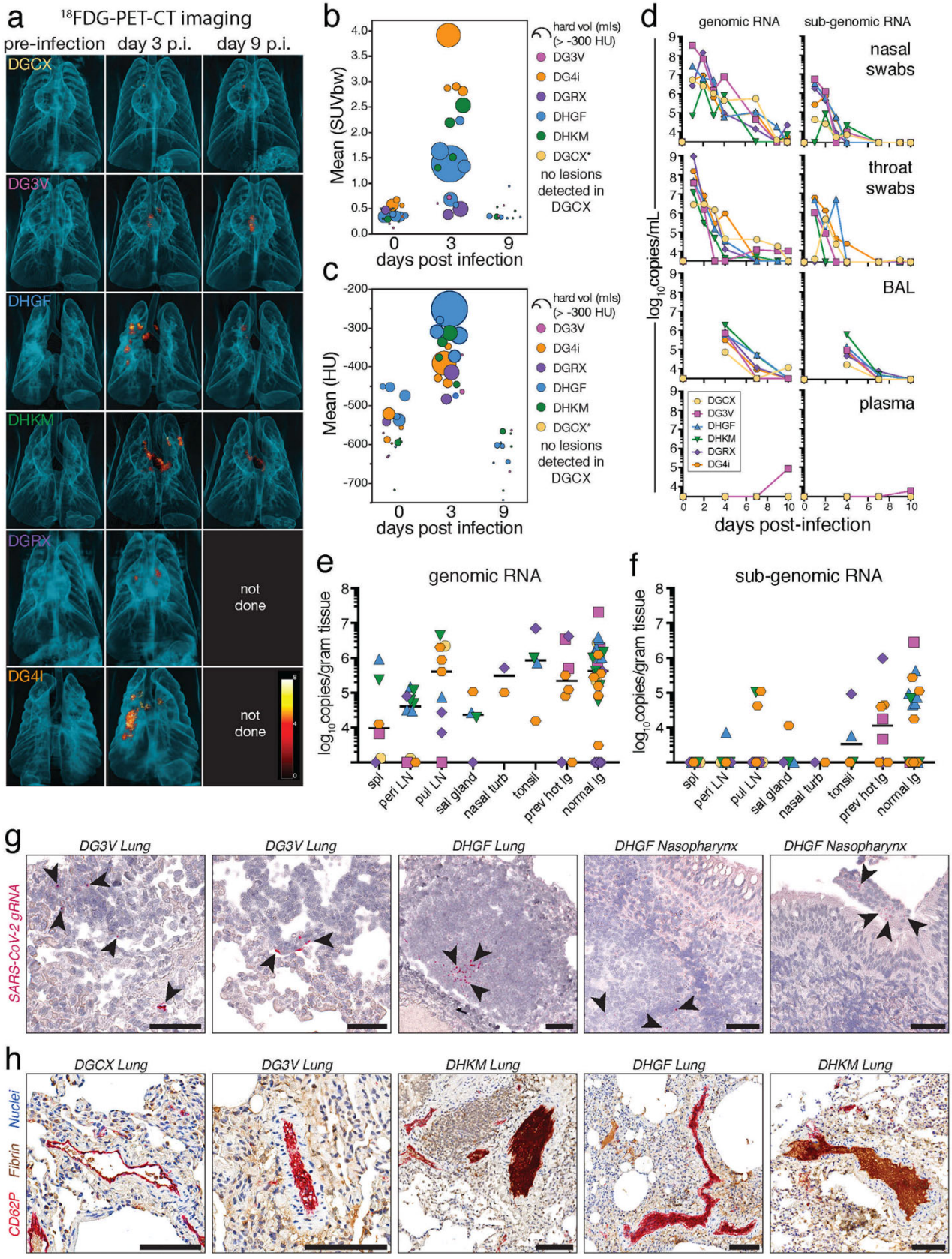
a
18FDG-PET-CT imaging
pre-infection
day 3 p.i.
day 9 p.i.
DGCX
DG3V
DHGF
DHKM
DGRX
DG4I
not done
not done
b
Mean (SUVbw)
days post infection
hard vol (mls) (> -300 HU)
DG3V
DG4i
DGRX
DHGF
DHKM
DGCX*
no lesions detected in DGCX
c
Mean (HU)
days post infection
hard vol (mls) (> -300 HU)
DG3V
DG4i
DGRX
DHGF
DHKM
DGCX*
no lesions detected in DGCX
d
genomic RNA
sub-genomic RNA
nasal swabs
throat swabs
BAL
plasma
log10copies/mL
days post-infection
DGCX
DG3V
DHGF
DHKM
DGRX
DG4i
e
genomic RNA
log10copies/gram tissue
spl
peri LN
pul LN
sal gland
nasal turb
tonsil
prev hot Ig
normal Ig
f
sub-genomic RNA
log10copies/gram tissue
spl
peri LN
pul LN
sal gland
nasal turb
tonsil
prev hot Ig
normal Ig
g
SARS-CoV-2 gRNA
DG3V Lung
DG3V Lung
DHGF Lung
DHGF Nasopharynx
DHGF Nasopharynx
h
Nuclei
Fibrin
CD62P
DGCX Lung
DG3V Lung
DHKM Lung
DHGF Lung
DHKM Lung

Fig. 1. Mild disease and rapid viral clearance in rhesus macaques infected with SARS-CoV-2. Six rhesus macaques infected with $2x10^6$ $TCID_{50}$ of SARS-CoV-2/WA-1 intranasally ($1x10^6$) and intratracheally ($1x10^6$). (A) 3D rendering of lung ^{18}FDG-PET/CT images pre-infection, day 3 and 9 post-infection. (B) Quantification of the metabolic activity (mean ^{18}FDG SUV) and volume of tissue with >-300 Houndsfield units (HU) (size of dot) from individual lesions, based on volumes of interest (VOI) defined at day 3 post-infection. (C) Quantification of density (mean HU) and volume of tissue with > -300 HU (size of dot) from individual lesions, based on VOI defined day 3 post-infection. DGCX did not have any detectable lung lesions. DGRX and DG4i did not have PET/CT imaging done at day 9 post-infection. (D) Quantification of viral genomic RNA (left column) and subgenomic RNA (right column) of the N gene from nasal swabs, throat swabs, BAL, and plasma in copies/mL by RT-qPCR. Cutoff for positivity for genomic RNA is 3000 copies/mL, cutoff for subgenomic RNA is 2500 copies/mL (nasal/throat) or 3000 copies/mL (BAL/plasma). (E-F) Quantification of viral genomic RNA (E) and subgenomic RNA (F) of the N gene from tissues at day 10 post-infection in copies/gram of tissue by RT-qPCR with individual samples and median. Cutoff for genomic RNA is 1000 copies/gram tissues, cutoff for subgenomic RNA is 1000 copies/gram tissue. (G) Representative images of staining for SARS-CoV-2 genomic RNA by RNA scope from the lung and nasopharynx at day 10 post-infection. Red is viral RNA. Scale bars are 50 microns. (H) Representative images of clotting patterns in the lung at day 10 post-infection. Red is platelet staining for CD62P, brown is fibrin, and blue are nuclei. Scale bars are 100 microns.

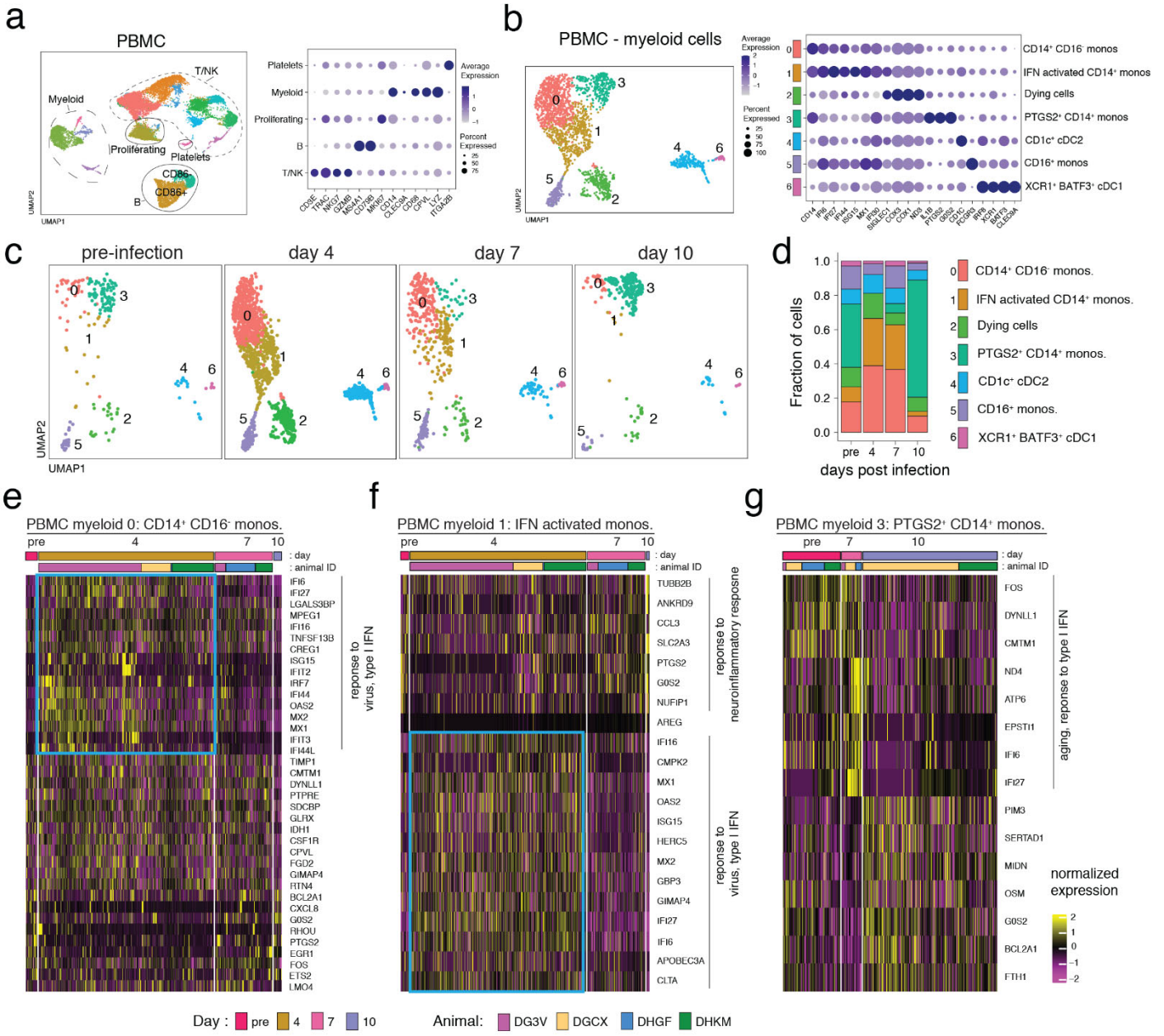

Fig. 2. Rapid and transient alterations in CD14⁺ monocytes in PBMCs after SARS-CoV-2 infection. (A) UMAP plot representing the clustering pattern of cells from scRNA-seq data of PBMCs from 4 animals (DGCX, DG3V, DHGF, and DHKM) (left panel). Each dot denotes a cell and is colored based on automated cluster identification. Clusters of cells belonging to a certain cell-type are demarcated and indicated on the plot. Expression levels of cell type defining markers are shown as a dot plot (right panel). Color intensity and dot size represent level of expression and percent of cells in that cluster expressing the gene as defined in the key. (B) UMAP representation of the sub-clustering of the myeloid cells from *A*. Clusters were annotated with cell-types based on gene expression patterns as shown on the dot plot and are identified with different numbers and colors on the plots. (C) UMAP plots separated by time depict the kinetic of the myeloid cells characterized in *B* at pre-infection, and day 4, 7, and 10 post-infection. (D) Fraction of cells that comprise each myeloid cell-type for each of the 4 timepoints shown in *C* is summarized. (E-G). Heatmap represents the hierarchical clustering of normalized expression levels of differentially expressed genes for each cell for three myeloid clusters. The cluster names are indicated on top of the heatmap and the first and second color bars distinguish time point and animal respectively. Genes were considered differentially expressed between timepoints if log fold change ≥ 0.5 and adjusted p-value < 0.01. Biological processes associated with the genes are indicated on the side and the blue box highlights type I IFN-responsive genes up-regulated at day 4.

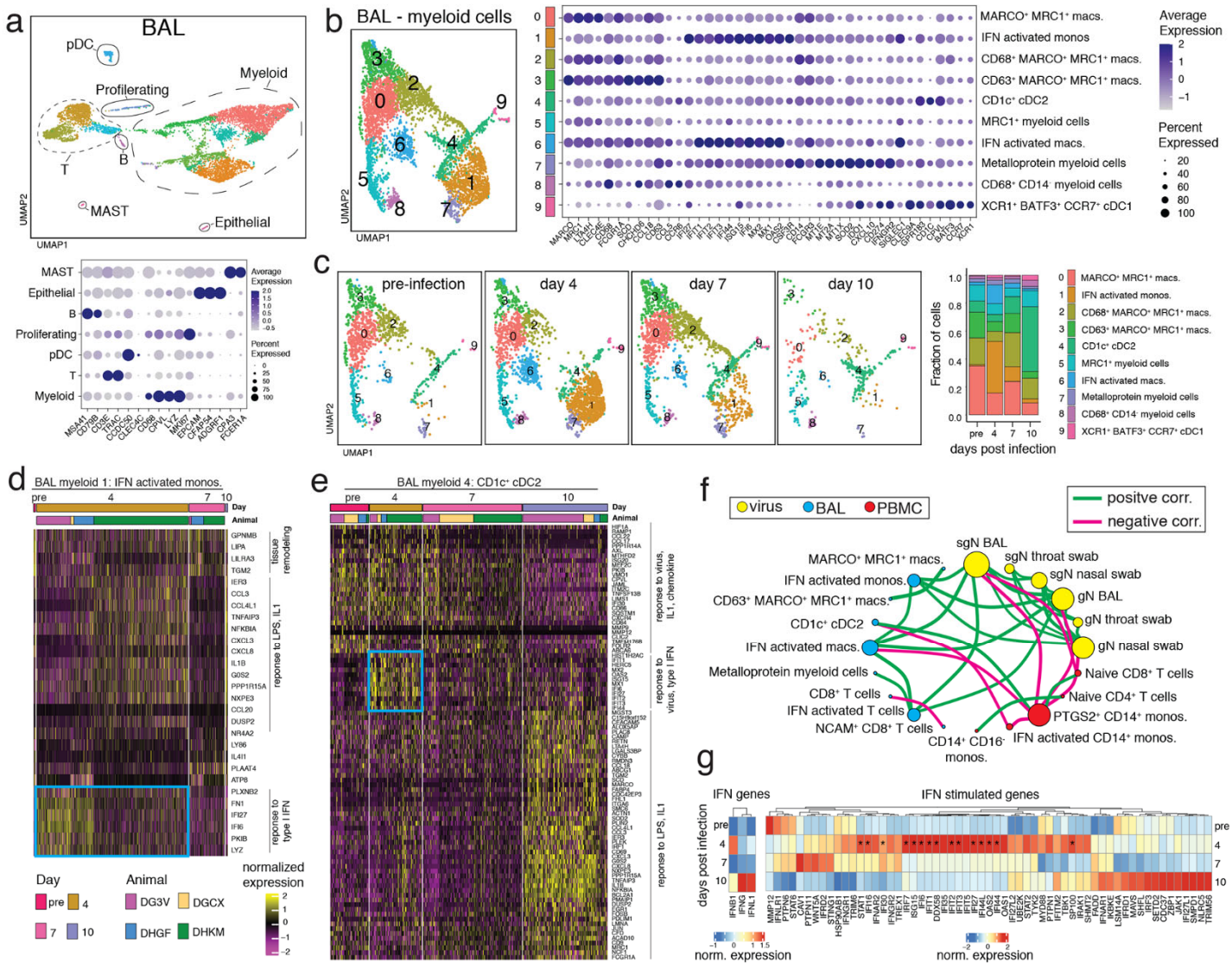
a
BAL
pDC
Myeloid
Profilerating
T
B
MAST
Epithelial
UMAP1
UMAP2
MAST
Epithelial
B
Proliferating
pDC
T
Myeloid
Average Expression
Percent Expressed
b
BAL - myeloid cells
MARCO⁺ MRC1⁺ macs.
IFN activated monos
CD68⁺ MARCO⁺ MRC1⁺ macs.
CD63⁺ MARCO⁺ MRC1⁺ macs.
CD1c⁺ cDC2
MRC1⁺ myeloid cells
IFN activated macs.
Metalloprotein myeloid cells
CD68⁺ CD14⁻ myeloid cells
XCR1⁺ BATF3⁺ CCR7⁺ cDC1
Average Expression
Percent Expressed
c
pre-infection
day 4
day 7
day 10
Fraction of cells
days post infection
d
BAL myeloid 1: IFN activated monos.
Day
Animal
tissue remodeling
reponse to LPS, IL1
reponse to type I IFN
normalized expression
e
BAL myeloid 4: CD1c⁺ cDC2
reponse to virus, IL1, chemokine
reponse to virus, type I IFN
reponse to LPS, IL1
f
virus
BAL
PBMC
positve corr.
negative corr.
sgN BAL
sgN throat swab
sgN nasal swab
gN BAL
gN throat swab
gN nasal swab
Naive CD8⁺ T cells
Naive CD4⁺ T cells
PTGS2⁺ CD14⁺ monos.
IFN activated CD14⁺ monos.
CD14⁺ CD16⁻ monos.
NCAM⁺ CD8⁺ T cells
IFN activated T cells
CD8⁺ T cells
Metalloprotein myeloid cells
IFN activated macs.
CD1c⁺ cDC2
CD63⁺ MARCO⁺ MRC1⁺ macs.
IFN activated monos.
MARCO⁺ MRC1⁺ macs.
g
IFN genes
IFN stimulated genes
days post infection
norm. expression
norm. expression

Fig. 3. Myeloid cell activation in the airways after SARS-CoV-2 infection. (A) UMAP plot of scRNAseq data from BAL of 4 rhesus macaques (DGCX, DG3V, DHGF, and DHKM) (top panel). Cell clusters are annotated based on broad cell-types and are circled and indicated on the plot. Each dot represents a cell and is colored by cluster. Dot plot displays expression level of markers used to identify the cell types (lower panel). Color intensity and dot size represent level of expression and percent of cells in that cluster expressing the gene marker as defined in the key. (B) UMAP plot (left) of the sub-clustering of the myeloid cells from *A*. Clusters were annotated with cell-types based on gene expression patterns as shown on the dot plot and are identified with different numbers and colors on the plots. (right). (C) UMAP plots depict the kinetic of myeloid cells over time (left) and the fraction of cells that compromise each cluster at pre-infection, and day 4, 7, and 10 post-infection is summarized as the bar plot (right). (D-E) Normalized gene expression from cells of two BAL myeloid clusters is visualized as a hierarchically clustered heatmap. The timepoints and animals are indicated as colored bars above the heatmap and are defined in the color key. Only genes that were differentially expressed between timepoints (log fold change ≥ 0.5 and adjusted p-value < 0.01) are shown. Biological processes associated with the genes are indicated on the side and the blue box highlights type I IFN-responsive genes up-regulated at day 4. (F) Spearman's correlation matrix based on the kinetics of viral loads and fraction of cells from BAL and PBMC myeloid and lymphoid clusters was calculated and visualized as a correlation network. Each circle represents a parameter with the different colors indicating a viral, BAL or PBMC cluster parameter. The size of the circle is proportional to the number of significant correlations (adjusted $p < 0.05$). A connecting line between two parameters indicates a significant correlation with green and pink lines signifying a positive and negative correlation respectively. (G) Average expression of IFN and IFN-stimulated genes from all BAL cells separated by time is clustered and represented as a heatmap. Genes that show a significant difference (adjusted $p < 0.05$) in expression over time are indicated with *.

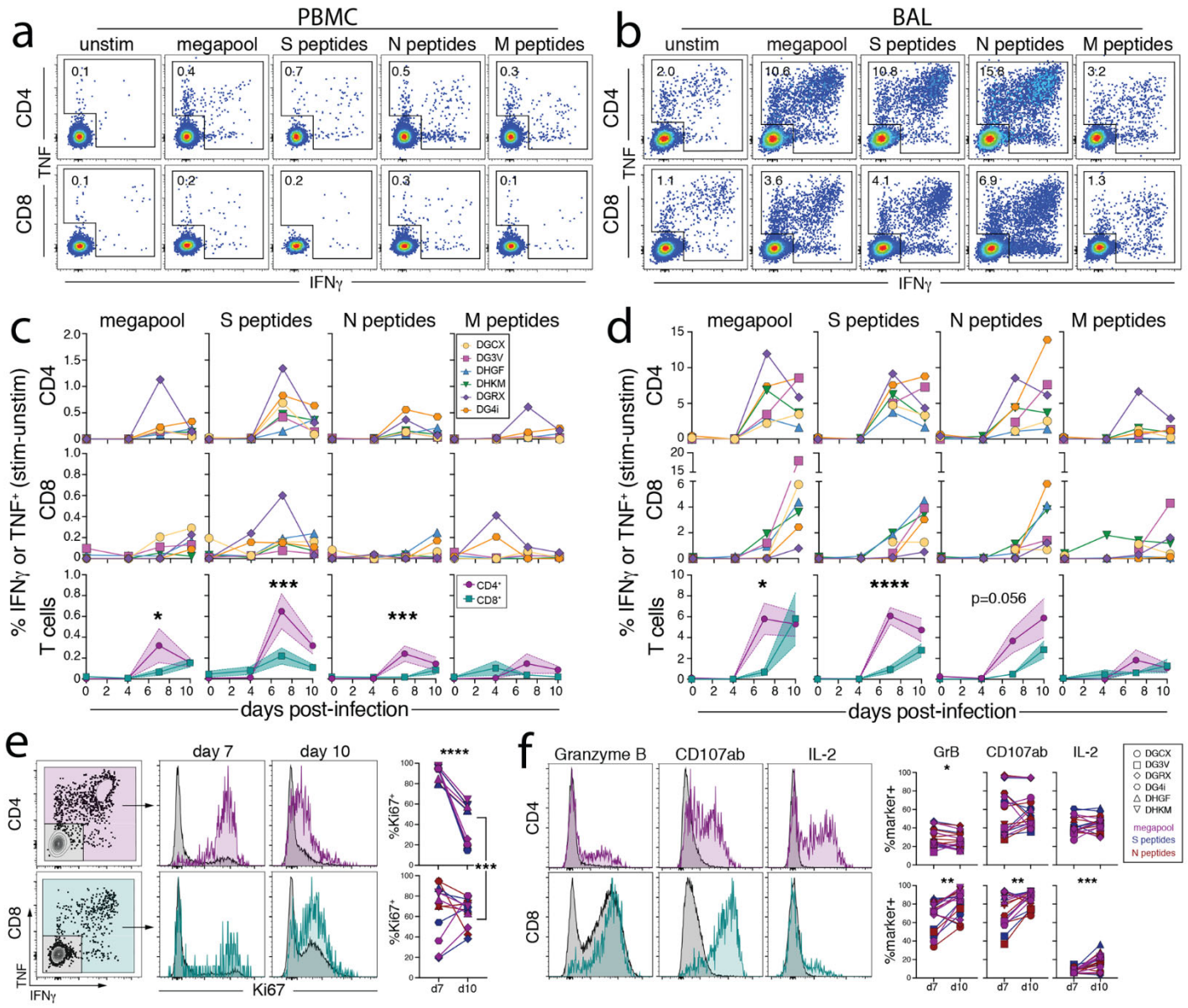
a
PBMC
unstim
megapool
S peptides
N peptides
M peptides
CD4
CD8
TNF
IFNγ
0.1
0.4
0.7
0.5
0.3
0.1
0.2
0.2
0.3
0.1
b
BAL
2.0
10.6
10.8
15.8
3.2
1.1
3.6
4.1
6.9
1.3
c
megapool
S peptides
N peptides
M peptides
% IFNγ or TNF+ (stim-unstim)
CD4
CD8
T cells
DGCX
DG3V
DHGF
DHKM
DGRX
DG4i
CD4+
CD8+
*
***
***
days post-infection
d
megapool
S peptides
N peptides
M peptides
*
****
p=0.056
days post-infection
e
CD4
CD8
TNF
IFNγ
day 7
day 10
Ki67
%Ki67+
****
***
d7
d10
f
Granzyme B
CD107ab
IL-2
GrB
CD107ab
IL-2
%marker+
*
**
**
***
DGCX
DG3V
DGRX
DG4i
DHGF
DHKM
megapool
S peptides
N peptides

Fig. 4. Kinetics of SARS-COV-2-specific CD8⁺ and CD4⁺ T cell responses in the airways. (A-D) Ag-specific CD8⁺ and CD4⁺ T cell responses in the blood and BAL enumerated by production of cytokines (IFN_γ and/or TNF) after ex vivo peptide stimulation with peptide pools to Spike (S), Nucleocapsid (N), Membrane (M), and an optimized SARS-CoV-2 peptide megapool (See Methods for description of peptides). Representative flow cytometry plots of Ag-specific CD8⁺ and CD4⁺ T cells from ID#DG4i at day 10 post-infection from unstimulated, megapool, S, N, and M peptides from blood (A) and BAL (B), gated on activated T cells i.e., $CD8^+CD95^+$ or $CD4^+CD95^+$. Quantification of Ag-specific T cells from all animals over time in blood (C) and BAL (D), calculated by subtracting the frequency of IFN_γ^+ and/or TNF^+ in the unstimulated samples from the frequency in the stimulated samples. Bottom row of graphs is an overlay of the mean CD8 and CD4 Ag-specific responses with standard error and a 2-way ANOVA with a Sidaks's multiple comparison test of CD4 vs. CD8 responses at each timepoint. DGCX and DG3V do not have quantification of S, N, and M responses from BAL at day 4, and are only represented by megapool at day 4. (E) Representative flow cytometry plots of Ki67 expression by Ag-specific CD8⁺ and CD4⁺ T cells from the BAL after S peptide stimulation at day 7 and day 10 post-infection from ID#DG4i. Graphs indicate the percent $Ki67^+$ of Ag-specific CD8⁺ and CD4⁺ T cells responding to megapool, S, and N peptides from BAL at day 7 and day 10 post-infection. Only samples with >35 data points were included. Paired *t* test of day 7 vs. day 10 for CD8 and CD4 separately, and CD8 day 10 vs. CD4 day 10. Ki67 staining was not done for ID#DGCX and DG3V. (F) Representative flow cytometry plots of Granzyme B, CD107a/b, and IL-2 expression by Ag-specific CD8⁺ and CD4⁺ T cells from the BAL after S peptide stimulation at day 7 and day 10 post-infection from ID#DG4i. Graphs indicate the percent Granzyme B^+, $CD107a/b^+$, or $IL\text{-}2^+$ of Ag-specific CD8⁺ and CD4⁺ T cells responding to megapool, S, and N peptides from BAL at day 7 and day 10 post-infection. Only samples with >35 data points were included. Paired *t* test of day 7 vs. day 10 for CD8 and CD4 separately. For all statistical analysis $p<0.05$ for the given test is considered significant: * $p<0.05$, ** $p<0.01$, *** $p<0.001$, **** $p<0.0001$.

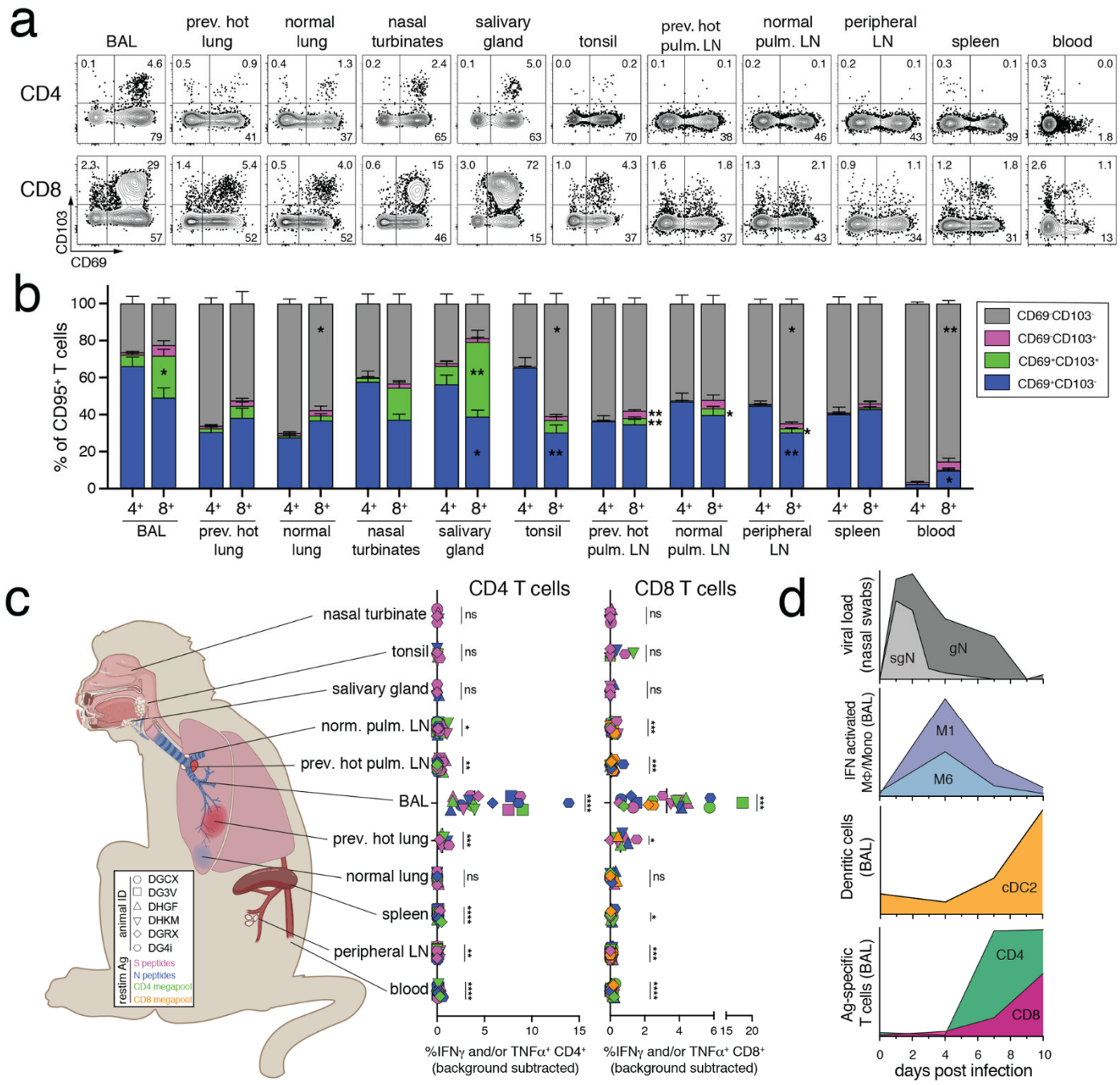
a
BAL
prev. hot lung
normal lung
nasal turbinates
salivary gland
tonsil
prev. hot pulm. LN
normal pulm. LN
peripheral LN
spleen
blood
CD4
CD8
CD103
CD69
b
% of CD95⁺ T cells
CD69⁻CD103⁻
CD69⁻CD103⁺
CD69⁺CD103⁺
CD69⁺CD103⁻
4⁺ 8⁺
c
CD4 T cells
CD8 T cells
nasal turbinate
tonsil
salivary gland
norm. pulm. LN
prev. hot pulm. LN
BAL
prev. hot lung
normal lung
spleen
peripheral LN
blood
ns
animal ID
DGCX
DG3V
DHGF
DHKM
DGRX
DG4i
restim Ag
S peptides
N peptides
CD4 megapool
CD8 megapool
%IFNγ and/or TNFα⁺ CD4⁺ (background subtracted)
%IFNγ and/or TNFα⁺ CD8⁺ (background subtracted)
d
viral load (nasal swabs)
sgN
gN
IFN activated MΦ/Mono (BAL)
M1
M6
Denritic cells (BAL)
cDC2
Ag-specific T cells (BAL)
CD4
CD8
days post infection

Fig. 5. Distribution of SARS-CoV-2-specific effector CD8⁺ and CD4⁺ T cells in mucosal tissues. (A-B) CD69 and CD103, and antigen-specific T cell responses after ex vivo peptide stimulation from secondary lymphoid organs and non-lymphoid tissues at day 10 post-infection. (A) Representative flow cytometry plots of CD69 and CD103 expression on $CD8^+CD95^+$ or $CD4^+CD95^+$ from BAL, previously hot lung sections, normal lung sections, nasal turbinates, salivary gland (parotid), tonsil, previously hot pulmonary lymph node, normal pulmonary lymph node, peripheral lymph node (axillary), spleen, and blood from ID#DHGF in unstimulated samples at day 10 post-infection. (B) Enumeration of percent $CD69^+$ and $CD103^+$ of $CD8^+CD95^+$ or $CD4^+CD95^+$ in unstimulated samples. Peripheral lymph node includes axillary, inguinal, and cervical lymph nodes. Previously hot lung sections not done for DGCX and DG3V. Sidak's multiple comparison test for values on $CD8^+$ vs. CD^+4 T cells for each tissue. (C) Tissue distribution diagram and quantification of the frequency of Ag-specific (IFN_γ^+ and/or TNF^+) in $CD4^+CD95^+$ (left graph) or $CD8^+CD95^+$ (right graph) in each tissue against peptide pools for Spike (S), Nucleocapsid (N), Membrane (M), and an optimized SARS-CoV-2 peptide megapools for $CD4^+$ and $CD8^+$ T cells (See Methods for description of peptides). Frequency calculated by subtracting the frequency of IFN_γ^+ and/or TNF^+ in the unstimulated samples from the frequency in the stimulated samples. Statistics are paired *t* tests of stimulated vs. unstimulated for each condition. Ag-specific T cells from BAL at day 10, was shown in Fig. 4, with addition of CD8 megapool here. Tissue graphic created with BioRender.com. (D) Representative summary graphs of the immune response to SARS-CoV-2 infection in rhesus macaques. Median genomic and subgenomic viral RNA levels from nasal swabs on a log scale, as in Fig. 1. Mean frequency of myeloid subpopulation 1 and 6 in BAL, as in Fig. 3. Mean frequency of cDC2 (BAL myeloid subpopulation 4) in BAL, as in Fig. 3. Mean frequency of the sum of Ag-specific $CD4^+$ and $CD8^+$ T cells (S+N+M peptide pools) in BAL, as in Fig. 4. For all statistical analysis $p<0.05$ for the given test is considered significant: * $p<0.05$, ** $p<0.01$, *** $p<0.001$, **** $p<0.0001$.